DTU Library

The NuSTAR Extragalactic Surveys: Initial Results and Catalog from the Extended Chandra Deep Field South

Mullaney, J. R.; Del-Moro, A.; Aird, J.; Alexander, D. M.; Civano, F. M.; Hickox, R. C.; Lansbury, G. B.; Ajello, M.; Assef, R.; Ballantyne, D. R.

Total number of authors:
36

THE *NuSTAR* EXTRAGALACTIC SURVEYS: INITIAL RESULTS AND CATALOG FROM THE EXTENDED *CHANDRA* DEEP FIELD SOUTH

J. R. Mullaney[1,2], A. Del-Moro[1], J. Aird[1,3], D. M. Alexander[1], F. M. Civano[4,5,6], R. C. Hickox[6], G. B. Lansbury[1],
M. Ajello[7], R. Assef[8], D. R. Ballantyne[9], M. Baloković[10], F. E. Bauer[11,12,13], W. N. Brandt[14,15,16], S. E. Boggs[7],
M. Brightman[10], F. E. Christensen[17], A. Comastri[18], W. W. Craig[7], M. Elvis[19], K. Forster[10], P. Gandhi[1,20],
B. W. Grefenstette[10], C. J. Hailey[21], F. A. Harrison[10], M. Koss[22], S. M. LaMassa[4], B. Luo[14,15], K. K. Madsen[10],
S. Puccetti[23,24], C. Saez[25], D. Stern[26], E. Treister[27], C. M. Urry[4], D. R. Wik[28,29], L. Zappacosta[24], and W. Zhang[30]

[1] Centre of Extragalactic Astronomy, Department of Physics, Durham University, South Road, Durham DH1 3LE, UK
[2] The Department of Physics and Astronomy, The University of Sheffield, Hounsfield Road, Sheffield S3 7RH, UK
[3] Institute of Astronomy, University of Cambridge, Madingley Road, Cambridge CB3 0HA, UK
[4] Yale Center for Astronomy and Astrophysics, 260 Whitney Avenue, New Haven, CT 06520, USA
[5] Smithsonian Astrophysical Observatory, 60 Garden Street, Cambridge, MA 02138, USA
[6] Department of Physics and Astronomy, Dartmouth College, 6127 Wilder Laboratory, Hanover, NH 03755, USA
[7] Space Sciences Laboratory, 7 Gauss Way, University of California, Berkeley, CA 94720-7450, USA
[8] Núcleo de Astronomía de la Facultad de Ingeniería, Universidad Diego Portales, Av. Ejército Libertador 441, Santiago, Chile
[9] Center for Relativistic Astrophysics, School of Physics, Georgia Institute of Technology, Atlanta, GA 30332, USA
[10] Cahill Center for Astrophysics, 1216 E. California Boulevard, California Institute of Technology, Pasadena, CA 91125, USA
[11] Instituto de Astrofísica, Facultad de Física, Pontificia Universidad Católica de Chile, 306, Santiago 22, Chile
[12] Millennium Institute of Astrophysics, Santiago, Chile
[13] Space Science Institute, 4750 Walnut Street, Suite 205, Boulder, CO 80301, USA
[14] Department of Astronomy and Astrophysics, The Pennsylvania State University, 525 Davey Lab, University Park, PA 16802, USA
[15] Institute for Gravitation and the Cosmos, The Pennsylvania State University, University Park, PA 16802, USA
[16] Department of Physics, The Pennsylvania State University, University Park, PA 16802, USA
[17] DTU Space, National Space Institute, Technical University of Denmark, Elektrovej 327, DK-2800 Lyngby, Denmark
[18] INAF Osservatorio Astronomico di Bologna, via Ranzani 1, I-40127, Bologna, Italy
[19] Harvard Smithsonian Center for Astrophysics, 60 Garden Street, Cambridge, MA 02138, USA
[20] School of Physics & Astronomy, University of Southampton, Highfield, Southampton SO17 1BJ, UK
[21] Columbia Astrophysics Laboratory, Columbia University, New York, NY 10027, USA
[22] Institute for Astronomy, Department of Physics, ETH Zurich, Wolfgang-Pauli-Strasse 27, CH-8093 Zurich, Switzerland
[23] ASDC-ASI, Via del Politecnico, I-00133 Roma, Italy
[24] Osservatorio Astronomico di Roma (INAF), via Frascati 33, I-00040 Monte Porzio Catone (Roma), Italy
[25] Department of Astronomy, University of Maryland, College Park, MD 20742-2421, USA
[26] Jet Propulsion Laboratory, California Institute of Technology, 4800 Oak Grove Drive, Mail Stop 169-221, Pasadena, CA 91109, USA
[27] Universidad de Concepción, Departamento de Astronomía, Casilla 160-C, Concepción, Chile
[28] NASA Goddard Space Flight Center, Code 662, Greenbelt, MD 20771, USA
[29] The Johns Hopkins University, Homewood Campus, Baltimore, MD 21218, USA
[30] Physics & Engineering Department, West Virginia Wesleyan College, Buckhannon, WV 26201, USA

ABSTRACT

We present the initial results and the source catalog from the *Nuclear Spectroscopic Telescope Array* (*NuSTAR*) survey of the Extended *Chandra* Deep Field South (hereafter, ECDFS)—currently the deepest contiguous component of the *NuSTAR* extragalactic survey program. The survey covers the full $\approx 30' \times 30'$ area of this field to a maximum depth of ≈ 360 ks (≈ 220 ks when corrected for vignetting at 3–24 keV), reaching sensitivity limits of $\approx 1.3 \times 10^{-14}$ erg s^{-1} cm^{-2} (3–8 keV), $\approx 3.4 \times 10^{-14}$ erg s^{-1} cm^{-2} (8–24 keV), and $\approx 3.0 \times 10^{-14}$ erg s^{-1} cm^{-2} (3–24 keV). A total of 54 sources are detected over the full field, although five of these are found to lie below our significance threshold once contaminating flux from neighboring (i.e., blended) sources is taken into account. Of the remaining 49 that are significant, 19 are detected in the 8–24 keV band. The 8–24 to 3–8 keV band ratios of the 12 sources that are detected in both bands span the range 0.39–1.7, corresponding to a photon index range of $\Gamma \approx 0.5-2.3$, with a median photon index of $\overline{\Gamma} = 1.70 \pm 0.52$. The redshifts of the 49 sources in our main sample span the range $z = 0.21-2.7$, and their rest-frame 10–40 keV luminosities (derived from the observed 8–24 keV fluxes) span the range $L_{10-40\,\mathrm{keV}} \approx (0.7-300) \times 10^{43}$ erg s^{-1}, sampling below the "knee" of the X-ray luminosity function out to $z \sim 0.8-1$. Finally, we identify one *NuSTAR* source that has neither a *Chandra* nor an *XMM-Newton* counterpart, but that shows evidence of nuclear activity at infrared wavelengths and thus may represent a genuine, new X-ray source detected by *NuSTAR* in the ECDFS.

1. INTRODUCTION

Extragalactic X-ray surveys have revolutionized our understanding of the accretion of matter into supermassive black holes. Collectively they have provided a census of active galactic nuclei (AGNs) across broad swathes of parameter space, enabling astronomers to relate black hole growth to fundamental properties such as large-scale environment and host galaxy characteristics (e.g., stellar mass, age, morphology; see the reviews of Alexander & Hickox 2012; Brandt & Alexander 2015). Indeed, the deepest *Chandra* and *XMM-Newton* surveys identify significant populations (i.e., tens of) AGNs beyond $z \sim 3$ (e.g., Alexander et al. 2003; Hasinger 2008; Luo et al. 2008; Brusa et al. 2009; Elvis et al. 2009; Laird et al. 2009; Xue et al. 2011; Civano et al. 2012; Goulding et al. 2012; Ranalli et al. 2013), probing the history of black hole growth over $\gtrsim 80\%$ of the age of the universe. Such surveys have resolved almost all ($\approx 70\%$–90%) of the cosmic X-ray background (hereafter, CXB; Giacconi et al. 1962) at 0.5–8 keV (e.g., Worsley et al. 2005; Hickox & Markevitch 2006; Lehmer et al. 2012; Xue et al. 2012).

Despite their undeniable success in identifying and characterizing the AGN population to high redshifts, *Chandra* and *XMM-Newton* are only sensitive to observed-frame photon energies $\lesssim 10$ keV. This represents a significant limitation because it is known from earlier, nonfocusing X-ray missions that the CXB peaks at ≈ 20–40 keV (e.g., Marshall et al. 1980; Gruber et al. 1999; Churazov et al. 2007; Frontera et al. 2007; Ajello et al. 2008). Until recently, the most advanced X-ray telescopes sensitive to these energies have resolved only 1%–2% of this peak into individual sources (e.g., Krivonos et al. 2007; Ajello et al. 2008; Bottacini et al. 2012). As such, the sources that make up the peak of the CXB are almost wholly unconstrained by direct observations, with the best constraints instead coming from population synthesis models (i.e., using spectral models to extrapolate the X-ray spectra of the source populations detected at lower energies (e.g., Setti & Woltjer 1989; Madau et al. 1994; Comastri et al. 1995; Gilli et al. 2001, 2007; Treister & Urry 2005; Treister et al. 2009; Ballantyne et al. 2011). Many such models require a significant population of Compton-thick AGNs (i.e., obscured by absorbing column densities, $N_{\mathrm{H}} > 1.5 \times 10^{24}$ cm^{-2}, the inverse of the Thomson cross section) to reproduce the peak of the CXB. However, these predictions are heavily influenced by the spectral assumptions used to extrapolate the X-ray spectra to >10 keV, and strong degeneracies exist between the assumed model parameters (e.g., Ballantyne et al. 2006; Gilli et al. 2007; Treister et al. 2009; Akylas et al. 2012).

Recent progress in characterizing the hard X-ray output from the AGN population has been made by studies exploiting data collected by the *INTEGRAL* and *Swift* telescopes (e.g., Krivonos et al. 2007; Ajello et al. 2008, 2012; Tueller et al. 2008; Burlon et al. 2011; Vasudevan et al. 2013). These studies report that ~5%–25% of local AGNs are confirmed on the basis of X-ray spectral analyses to be Compton thick (to $N_{\mathrm{H}} \sim 10^{25}$ cm^{-2}). However, the limited sensitivity of these telescopes means that they can only probe the most local ($\lesssim 100$ Mpc) AGNs to the depth needed to verify Compton-thick levels of absorption, leaving no constraints on the evolution of the absorbed fractions of AGNs. The *Nuclear Spectroscopic Telescope Array* (hereafter, *NuSTAR*; Harrison et al. 2013) is a factor of $\sim 10^2$ more sensitive than previous high-energy X-ray telescopes and is predicted to determine the makeup of 25%–35% of the CXB

(Ballantyne et al. 2011), allowing us to measure the contribution from heavily obscured AGNs over truly cosmological scales. To achieve this scientific goal, *NuSTAR* has undertaken four extragalactic surveys, spanning a range of different combinations of area and depth, with the deepest observations identifying more common, faint sources. The complementary shallower, wider surveys will cover rarer, more extreme sources. The tiers that make up the *NuSTAR* extragalactic survey are (1) a large area (currently covering ≈ 7 deg^2), mostly shallow serendipitous survey consisting of the areas around targeted sources (described in Alexander et al. 2013; B. Lansbury et al. 2015, in preparation), (2) a middepth (≈ 90 ks maximum unvignetted depth) survey of the 2 deg^2 Cosmic Evolution Survey (COSMOS; Scoville et al. 2007), described in Civano et al. (2015), and (3) two deep (≈ 360 ks maximum unvignetted depth), small area surveys of the ≈ 0.25 deg^2 Extended *Chandra* Deep Field South (hereafter, ECDFS; Lehmer et al. 2005, hereafter L05)—the focus of this study—and the ≈ 0.24 deg^2 Extended Groth Strip (i.e., *NuSTAR* analysis to be presented in J. Aird et al. 2015, in preparation). By concentrating on extragalactic fields, these surveys will give a census of hard X-ray sources that is unbiased by preselection, enabling the characterization of a significant sample of the "typical" population responsible for the bulk of the CXB. Indeed, *NuSTAR* has already demonstrated this capability in the case of the ECDFS source NuSTAR J033202–2746.8.[31] Prior to *NuSTAR*, the spectral properties of this source were incorrectly constrained, but it has since been shown to be a high-redshift QSO with a significant reflection component, despite being Compton thin (Del Moro et al. 2014). If such reflection is common within the obscured—but sub-Compton-thick—AGN population, it would have a significant impact on our understanding of the makeup of the CXB.

In this study, we describe the *NuSTAR* observations of the ECDFS that form one of the two deepest contiguous components of the *NuSTAR* extragalactic survey (see Section 2.1). In Section 2.2 we describe the data reduction and processing steps we took to form the final science, background, and exposure mosaics. In Section 2.3, we describe how we obtained our "blind" source catalog, the format of which is described in our Appendix. In Section 3 we describe the first results from this sample of sources, including derived properties such as source fluxes, spectral indices, and luminosities. We discuss constraints on the number of sources not detected by either *Chandra* or *XMM-Newton* in Section 4. In Section 5 we give a brief overview of the *NuSTAR*-detected sources in the context of the previously known X-ray sources in this field. Finally, in Section 6, we summarize our results. We adopt $H_0 = 71$ km s^{-1} Mpc^{-1}, $\Omega_{\mathrm{M}} = 0.27$, and $\Omega_{\Lambda} = 0.73$ and use the AB-magnitude system throughout (where appropriate).

2. OBSERVATIONS AND ANALYSES

The *NuSTAR* ECDFS survey consists of observations from two separate passes. Observations making up the first pass were taken between 2012 September and December, and those making up the second pass were taken roughly six months later, between 2013 March and April. The details of these observations, including aim points, roll angles, and useable exposure times, are provided in Table 1. In this section, we describe our observing

---

[31] We note that due to minor changes in our data reduction since the publication of Del Moro et al. (2014), the name of this source has been updated to *NuSTAR* J033202–2746.7 in our catalog. We note that these changes do not affect any of the scientific results of Del Moro et al. (2014).

Table 1
Details of the Individual Observations That Make Up the Two *NuSTAR* Passes of the ECDFS

(1)	(2)	(3)	(4)	(5)	(6)
Exp. ID	Obs. Date	R.A.	Decl.	Roll Angle	$t_{\rm Exp}$
1	2012 Sep 28	52.93	−27.97	85.28	44.9
2	2012 Sep 29	53.06	−27.97	85.30	45.6
3	2012 Sep 30	53.18	−27.97	85.30	47.1
4	2012 Oct 01	53.31	−27.97	85.31	47.0
5	2012 Oct 02	52.93	−27.86	85.30	46.3
6	2012 Oct 04	53.06	−27.86	85.31	45.4
7	2012 Nov 30	53.18	−27.86	264.99	47.9
8	2012 Dec 01	53.31	−27.86	264.96	48.0
9	2012 Dec 03	52.93	−27.75	266.96	46.7
10	2012 Dec 04	53.06	−27.75	266.94	47.7
11	2012 Dec 05	53.18	−27.75	266.93	48.0
12	2012 Dec 06	53.31	−27.75	266.88	48.4
13	2012 Dec 07	52.93	−27.64	266.92	48.8
14	2012 Dec 08	53.06	−27.64	266.94	49.2
15	2012 Dec 09	53.18	−27.64	266.94	49.4
16	2012 Dec 10	53.30	−27.64	266.95	46.5
17	2013 Mar 15	53.30	−27.64	351.82	48.6
18	2013 Mar 17	53.18	−27.64	351.81	48.9
19	2013 Mar 18	53.06	−27.64	351.83	48.6
20	2013 Mar 19	52.93	−27.64	351.84	46.1
21	2013 Mar 20	53.31	−27.75	351.83	46.4
22	2013 Mar 21	53.18	−27.75	351.84	46.1
23a	2013 Mar 22	53.06	−27.75	351.86	31.0
23b	2013 Mar 23	53.06	−27.75	351.88	15.2
24	2013 Mar 24	52.93	−27.75	356.88	45.7
25	2013 Mar 25	53.31	−27.86	356.88	46.0
26	2013 Mar 26	53.18	−27.86	356.89	45.9
27	2013 Mar 27	53.06	−27.86	1.97	45.4
28	2013 Mar 28	52.93	−27.86	1.95	45.4
29	2013 Mar 29	53.31	−27.97	1.94	45.3
30	2013 Mar 30	53.18	−27.97	1.93	45.2
31	2013 Mar 31	53.06	−27.97	1.93	45.2
32	2013 Apr 01	52.93	−27.97	1.95	45.0

Note. (1): Exposure ID. (2): Start date of the observation. (3)–(5): The aim point R.A. and decl. and roll angle of the observation. (6): The useable exposure time (in ks) of the observation after filtering out the flaring events. Flares only affected Exp. IDs 2, 3, 18, and 22 (see Section 2.2.1).

strategy and outline the steps taken to process and analyze the resulting data. We note that, in order to ensure consistency between the different components of the *NuSTAR* extragalactic surveys, a determined effort was made to follow the same analysis techniques for both the COSMOS (Civano et al. (2015)) and the ECDFS surveys wherever possible.

2.1. Observing Strategy

NuSTAR features two independent telescopes with corresponding focal plane modules (hereafter, referred to as FPMA and FPMB) that simultaneously observe the same patch of sky during each observation. Each focal plane has a $\approx 12' \times 12'$ field of view and consists of four CdZnTe detectors. The physical pixels are $12''$ on a side, with the scale subdivided into $2''.46$ pixels in the software. Whereas the detectors are sensitive to photon energies in the range 3–100 keV, the optics of the telescope limit this range to 3–78.4 keV.[32] The focusing optics

---

[32] See Harrison et al. (2013) for a detailed description of the *NuSTAR* telescope.
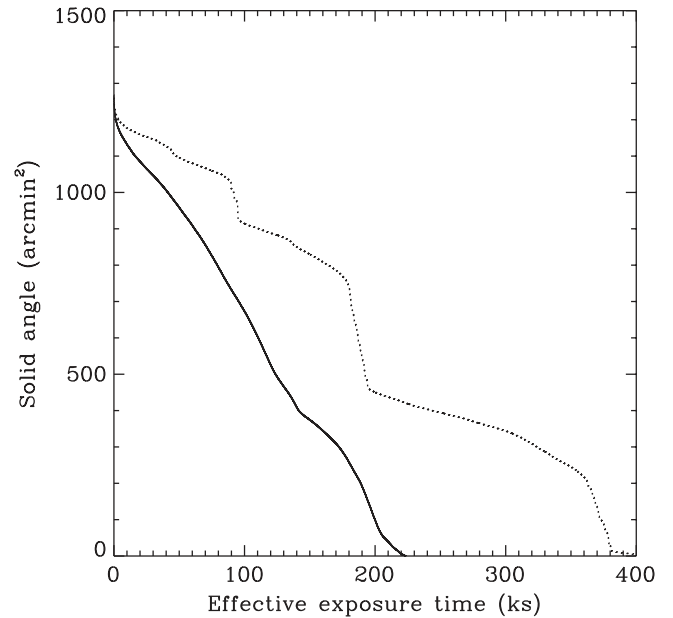

Figure 1. Cumulative area above a given exposure time in the 3–24 keV band for the final mosaic in a single focal plane module. The dotted line gives the total area above a given exposure before correcting for vignetting, whereas the solid line includes the effects of vignetting on the total exposure.

of *NuSTAR* give it an unprecedented angular resolution at these hard X-ray energies, with a tight central "core" of FWHM = $18''$ and a half-power diameter of $58''$, meaning surveys as deep as the ECDFS are not limited by confusion between detected sources. The area covered by the ECDFS (i.e., $\approx 30' \times 30'$; L05) is larger than the *NuSTAR* field of view, so we adopted a tiling strategy to provide full coverage of the field. A strategy of 16 pointings separated by a half-detector shift—forming a 4×4 square—was chosen based on the findings of presurvey tests, which suggested that this optimizes the number of detections in the field. Because the roll angle of the observatory is a function of time, the observing schedule was chosen not only to ensure that the edges of each observation were roughly aligned, but also to align them with the *Chandra* coverage of this field.

Each pointing had an effective exposure of approximately 45 ks per pass, and all but one of the pointings consisted of a single unbroken exposure, resulting in a total of 33 exposures.[33] Table 1 gives the precise useable integration times for each of the 33 separate exposures after filtering out flaring events (see Section 2.2.1). The total time spent on the ECDFS across both passes was 1.49 Ms. On completion of the two passes, the central, deepest $\approx 20' \times 20'$ region of the field was covered by eight separate pointings and was thus observed for a total of ~ 360 ks, and the edges had been covered by four pointings (i.e., to ~ 180 ks) and the corners by two (i.e., to ~ 90 ks). The cumulative area histogram showing the area of the sky covered to a given exposure time is shown in Figure 1.

2.2. Production of Science, Background, and Exposure Maps

In this subsection, we outline the detailed steps we took to produce the final mosaics, identify sources, and derive source

---

[33] Exp. ID 23 was split into two exposures of 31.0 and 15.2 ks each to accommodate a Target of Opportunity observation of the Galactic plane source NuSTAR J163433−4738.7; see Tomsick et al. (2014).

properties. All data reduction was performed using v6.15 of HEASoft, v1.3 of the *NuSTAR*-developed software, NuSTAR-DAS (included with v6.15 of HEASoft), and v4.5 of CIAO.[34]

2.2.1. Reprojection, Bad Pixel Rejection, Energy Bands

Each of the 33 exposures results in two event files, one each for FPMA and FPMB. These 66 raw, unfiltered event files were processed and reprojected using the NuSTARDAS program `nupipeline` to produce 66 clean event files. Inspection of the cleaned event files revealed that four exposures (Exp. IDs 2, 3, 18, and 22 in Table 1) had been significantly affected by flaring events. These events were filtered out using CIAO's `dmgti` tool to make a user-defined, good time-interval (gti) file, binning in 20 s intervals and rejecting periods when the average binned count rate exceeded 0.6 cts s^{-1} (within the whole observable energy range, i.e., 3–78.4 keV), a threshold selected through visual inspection of the light curves. This filtering removed a total of 6.0 ks of exposure time, representing ≈0.4% of the total exposure time for the two passes. Following Alexander et al. (2013), the final cleaned event files were split into three energy bands, 3–8, 8–24, and 3–24 keV, using HEASoft's `extractor` tool. The 24 keV upper band energy is chosen to optimize the signal-to-noise ratio (S/N) for sources with average spectral properties. For these sources, the combination of the photon spectrum falling rapidly with energy, a flat background, and a decreasing effective area means that the detection significance decreases with increasing high energy cutoff. As a check, we generated a fourth 24–40 keV band, but no significant sources were identified using the detection technique described below.

2.2.2. Background Map Generation

The majority of counts in all of the ECDFS observations are attributable to a background that arises from (1) an instrumental background component that dominates at energies ≳20 keV; (2) a focussed background component that is made up of X-ray emitting sources that are focussed by the telescope optics but lie below the detection threshold; (3) an "aperture" background that is astronomical in origin but is due to X-ray photons that have not scattered off (and thus have not been focussed by) the telescope optics; (4) a spatially uniform component that is strong at ≲5 keV, probably due to neutrons striking the detector; and (5) another low energy component that is related to solar photons reflecting off the back of the aperture stop. The aperture background dominates the photon counts at ≲30 keV and, as such, most strongly affects our chosen energy bands.

Due to the asymmetric layout of the optics bench, the aperture background has a strong gradient that differs between FPMA and FPMB, making it difficult to subtract by the usual process of extrapolating from regions around the source. This is especially true in the case of overlapping observations, such as those that make up the ECDFS mosaic. Instead, we use a model of the aperture background for each FPM produced using the specially developed IDL software `nuskybgd` (Wik et al. 2014). The X-ray spectrum is extracted from a set of user-defined background regions and then fit with a predefined model consisting of the five components listed above (note that

component [4] is incorporated into the instrumental background, i.e., component [1]). A set of predetermined maps that describe the spatial distribution of each background component in each energy band (see Wik et al. 2014) are then adjusted using the normalizations of the spectral fit.

When generating the model background, there is the option in `nuskybgd` to exclude known bright sources in each image from the user-defined regions to prevent them from being inappropriately included in the background estimation. We experimented with excluding known bright sources, but they were found to have no significant impact on either our final detected source list or source fluxes.[35] In light of this, and for reproducibility, we chose not to exclude sources in generating our final background maps. Instead, we simply used four large (i.e., ∼5′ on a side) square regions centered on the four chips that make up each detector to define our background regions (using the same procedure as for the *NuSTAR*-COSMOS survey described in Civano et al. (2015)).

A highly accurate synthetic background map is crucial in determining source reliability and calculating net source counts and, ultimately, fluxes. To test the reliability of the synthetic background maps, we calculated the relative difference between the number of counts extracted from 3,500 30″ radius regions distributed across the "synthetic" background and the number of counts extracted in the same regions distributed across the science mosaics (i.e., $(C_{\mathrm{Sci}} - C_{\mathrm{Bgd}})/C_{\mathrm{Sci}}$). The resulting values are normally distributed with a dispersion (σ) of 0.078, 0.064, and 0.053 centered around 1.7×10^{-3}, -1.9×10^{-3}, and -4.4×10^{-3} for the 3–8, 8–24, and 3–24 keV bands, respectively (FPMA and FPMB combined). Tests conducted on mock science images (i.e., Poissonian realizations of the background maps) demonstrated that this dispersion is consistent with that expected due to Poisson noise, meaning that the uncertainties introduced by the background estimation are small compared to those due to the noise in the data.

2.2.3. Exposure Maps and Vignetting

Exposure maps were generated using the NuSTARDAS software `nuexpomap`. As well as pointing information, this also takes into account the movement of *NuSTAR*'s 10 m long mast when determining the exposure time of each point on the sky translated into pixel position. To reduce processing time, there is the option to reduce the number of calculations by spatially binning the exposure maps. We therefore spatially bin our exposure maps over five pixels in each dimension, which is smaller than the 30″ aperture used for photometry measurements and thus has negligible influence on our flux measurements while speeding up processing by a factor of $\sim 5^2 = 25$.

The effects of vignetting were also taken into account with `nuexpomap` to generate effective exposure maps for each observation. The degree of vignetting is dependent on energy, but generating a vignetting map for every energy channel is prohibitive. Instead, following Civano et al. (2015), we calculated the energy that minimizes the difference across the three adopted energy bands by convolving the instrument response with a power-law spectrum of $\Gamma = 1.8$ (i.e., the average of nearby AGNs studied at >10 keV; Burlon et al. 2011). This results in three energies that we used to

---

[34] The HEASoft software is available to download via http://heasarc.gsfc.nasa.gov/lheasoft; the CIAO software is available to download via http://cxc.harvard.edu/ciao.

[35] The list of bright sources to exclude was generated using our source-detection algorithm with a background created *without* excluding any sources.

generate the effective exposure maps: 5.42 keV for the 3–8 keV band, 13.02 keV for the 8–24 keV band, and 9.88 keV for the 3–24 keV band. We calculate that this approximates the vignetting in each energy channel to within 14.5% for all three bands, the difference being largest farthest from the aim point. The effects of applying this vignetting correction are shown in Figure 1, in which the solid line shows the cumulative solid angle to a given effective exposure, evaluated at 3–24 keV. On average, correcting for vignetting reduces the nominal exposure time by a factor of about two.

2.2.4. Astrometric Correction

Before combining the individual observations to form the final science, exposure, and background mosaics, we experimented with correcting for astrometric offsets between individual exposures. In brief, we stacked the *NuSTAR* data at the positions of known *Chandra*-detected sources and used the relative positions of the stacked detected sources to perform first-order (i.e., *x*–*y* shift) astrometric corrections. However, we found that this correction had no measurable impact on either the list of detected sources or their measured fluxes. As such, we chose to not include any astrometric correction in the rest of our analyses in order to keep the analysis stream as simple as possible. Based on their analysis of simulated *NuSTAR* observations of the COSMOS field, Civano et al. (2015) estimate an average positional uncertainty of $6\rlap{.}''6$, which, due to the many similarities between the ECDFS and COSMOS *NuSTAR* survey strategies and data reduction, we adopt as the positional uncertainty for the detected ECDFS sources.

2.2.5. Mosaicking

To create a set of contiguous maps, the individual science, background, and exposure images were mosaicked using HEASoft's `ximage` package. Our experimentation with astrometry correction (see Section 2.2.4) demonstrated that the frames from both FPMA and FPMB are coaligned to within measurable tolerances, so we are able to combine the data from these two modules by adding the equivalent mosaics, thereby increasing the sensitivity of the final combined mosaic. The final mosaicked vignetting-corrected exposure map, combining FPMA and FPMB, is shown in Figure 2. All source-detection and derived photometric measurements are taken from the combination of the FPMA and FPMB mosaics.

2.3. Source Detection and Calculation of Derived Properties

In this subsection we detail how we produced our source catalog from the final science, background, and exposure maps. We adopted a multistage approach that successfully separates nearby sources and ensures that all significant sources are identified, while maintaining a low number of false-positive detections. The steps are as follows.

1. We first generate a seed list of potential sources in each band using our source detection procedure and a low significance detection threshold.
2. We combine the seed lists from each band using positional matching, and those not meeting our final, more stringent false-probability cut in any band are excised from the list to form our final catalog.
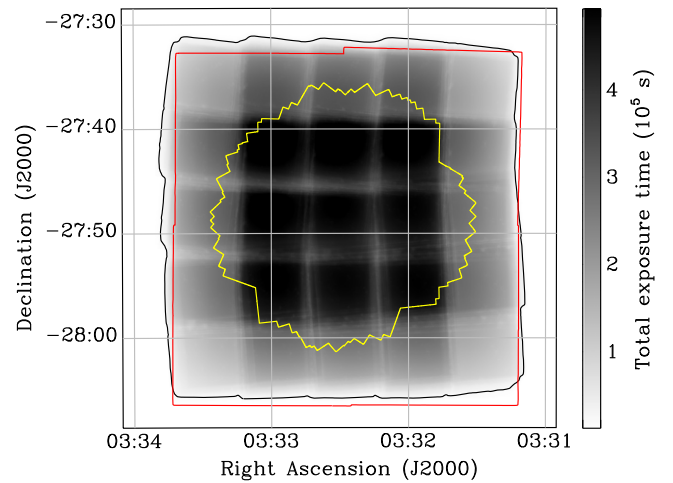

Figure 2. Vignetting-corrected exposure map showing the effective exposure of the field, combining both FPMA and FPMB. Darker grays imply longer effective exposures (see color bar). The black line shows the limit of the *NuSTAR* exposure, and the red and yellow lines show the limits of the 250 ks Chandra ECDFS (L05) and 4 Ms CDFS (Xue et al. 2011) exposures, respectively.

3. We perform aperture photometry at the positions of the sources in our final catalog.
4. We perform deblending (see Section 2.3.2) on the sources in the final catalog to account for the flux contribution from neighboring significant sources; those sources that prove to be below our significance threshold post-deblending are flagged but are retained in the final catalog.

A full description of each of these steps is provided below.

2.3.1. Initial Source Seed List

The strong, spatially varying background of the *NuSTAR* ECDFS mosaics (see Section 2.2.2) makes blind source detection challenging. Considerable testing with CIAO's `wavdetect` source-identification algorithm (Freeman et al. 2002) revealed that it is not designed to deal with the deep *NuSTAR* data in the ECDFS, and it identified large numbers (i.e., ~200) of false-positive detections, particularly in the outer regions of the field, likely due to the high background of *NuSTAR* images compared to the *Chandra* data for which `wavdetect` was originally developed to analyze. As a consequence, we instead employed the alternative approach of performing source detection directly on false-probability (hereafter, P_{False}) maps generated from the mosaics. These P_{False} maps, which we calculate using the incomplete gamma function (see Georgakakis et al. 2008), give the likelihood that the signal at each position in the mosaic is due to random fluctuations in the supplied background (i.e., not due to a real source). The maps were produced by passing smoothed science and background images to IDL's `igamma` function, which computes the incomplete gamma function at every position in the mosaics:

$$P_{\mathrm{False}} = \mathtt{igamma}(\mathrm{Sci},\ \mathrm{Bgd}), \qquad (1)$$

where Sci and Bgd are the smoothed science and background mosaics, respectively. Two different smoothing lengths composed of $10''$ and $20''$ radius top-hat functions were employed; the smaller radius helps separate adjacent sources,
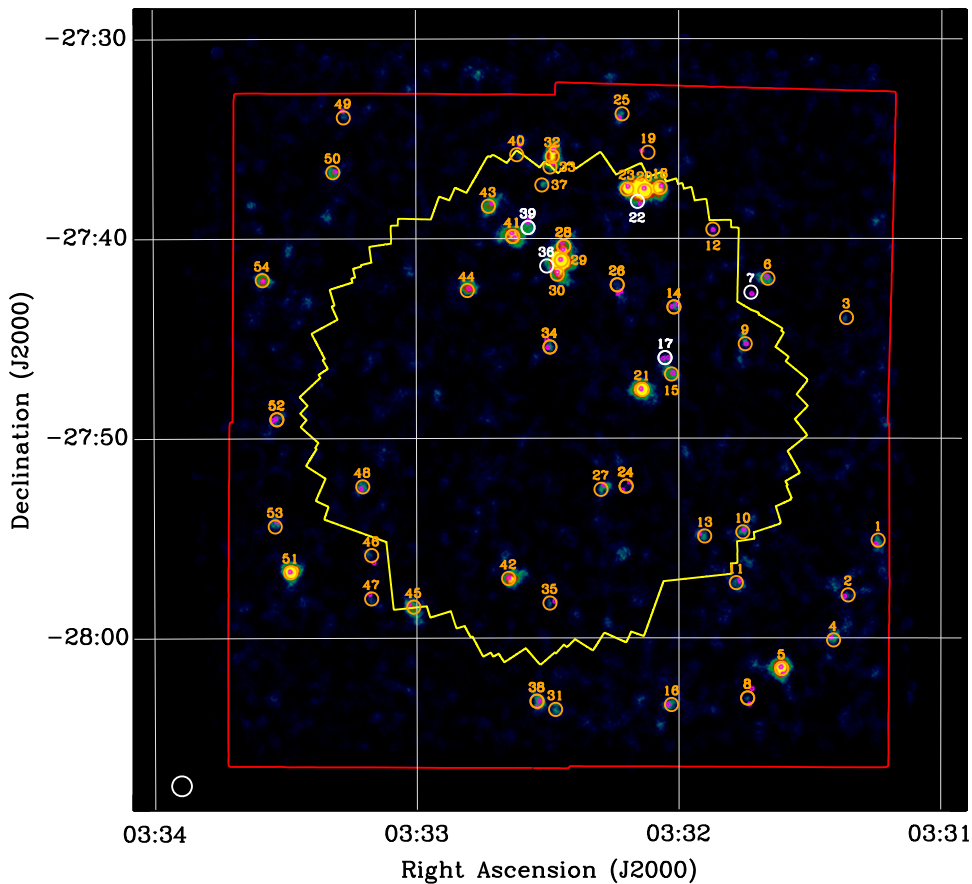
Figure 3. False-probability (P_{False}) map produced by combining data in the 3–24 keV band from both FPMA and FPMB. Blue, green, and yellow shading indicates areas of increasingly lower P_{False}, and thus the regions most likely to be associated with genuine sources. The yellow and red lines indicate the extent of the the 4 Ms CDFS (Xue et al. 2011) and 250 ks Chandra ECDFS (L05) surveys, respectively. The white circle in the bottom left of the figure indicates the size of the 30″-radius aperture used for measuring source photometry. The positions of all *NuSTAR* sources found using our detection algorithm (see Section 2.3.1) are indicated with small numbered circles (the numbers refer to the source ID in the online catalog). Orange circles indicate those that remain significant (i.e., meet our significance thresholds) after taking into account the effects of neighboring sources (after source deblending; see Section 2.3.2), whereas the white circles indicate those that no longer prove to be significant. Note that in some instances the position does not correspond to that of the minimum P_{False} in the 3–24 keV band. This is because those sources are detected at a higher significance in another band and, as such, the position is based on the minimum P_{False} position in that other band (see Section 2.3.1). Small magenta circles indicate the positions of the *Chandra* or *XMM-Newton* counterparts to the *NuSTAR*-detected sources.

whereas the larger helps to identify fainter sources. Smoothed P_{False} maps were generated for each of our three energy bands, and source detection was performed separately on each. Figure 3 shows the 20″-smoothed P_{False} map for the 3–24 keV band mosaic, while Figure 4 shows the same, but for the 8–24 keV band.

We used the SExtractor source-detection algorithm (Bertin & Arnouts 1996) to identify regions of the P_{False} maps below a given threshold. Because SExtractor is designed to identify peaks in an image, we provided the log of the inverse P_{False} maps as input. The SExtractor detection algorithm requires a number of input parameters, the most important of which for our purposes is the threshold above which (in the inverse map) a source is considered to be significant. Poisson realizations of the blank background maps (see Section 2.2.2) were used to set the thresholds in each band. These Poisson realizations were treated as input science images and analyzed using the same procedures as the real science maps. By running our source-detection algorithm on 100 realizations of these simulated, blank maps, we determined the P_{False} value below which we should expect, on average, one false-positive detection per ECDFS area per band and set those as our thresholds. This

corresponds to thresholds of $\log(P_{\mathrm{False}}) \leqslant -5.19$, $\leqslant -5.22$ and $\leqslant -5.34$ in the 3–8, 8–24, and 3–24 keV bands, respectively. We note that these thresholds correspond to $\approx 99\%$ reliability, as evaluated by the simulated *NuSTAR* observations described in Civano et al. (2015). Based on our Poisson realizations, there is a 34%, 42%, 19%, 3%, 1%, and 1% likelihood that the 3–24 keV band mosaic contains zero, one, two, three, four, and five false-positive detections (i.e., have $\log(P_{\mathrm{False}}) \leqslant -5.34$) .[36] For the generation of our seed catalog, we employ a somewhat more liberal threshold of $\log(P_{\mathrm{False}}) \leqslant -4.5$ in all three bands to ensure that we detect all potential sources, and we employ the more stringent thresholds in our final cut after combining sources detected in each band (see Section 2.3.2). Because the input maps have already been smoothed, we consider even a single pixel above these thresholds to be a potential source. The coordinates of each detection are taken as the position of the local minimum P_{False} (rather than, for

---

[36] The corresponding likelihoods for the 3–8 keV band are 38%, 33%, 24%, 4%, 0%, and 1%, and for the 8–24 keV band they are 42%, 32%, 18%, 4%, 3%, and 1%. We note that, in all bands, the likelihood-weighted number of false positives sum to one, confirming that the average number of false-positive detections per realization is one.
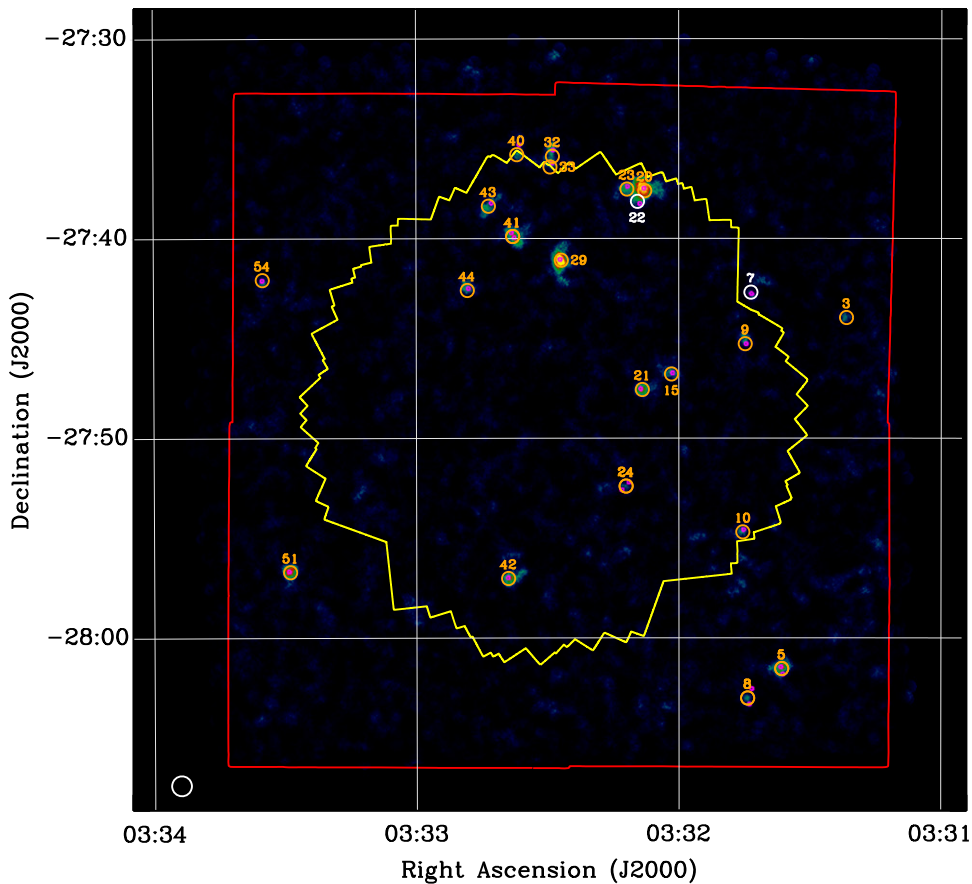
Figure 4. Same as Figure 3, but for the 8–24 keV band. The sources shown are only those that are detected in this band.

example, the centroid) to maximize the likelihood that it will satisfy our more stringent final threshold cuts.

Because we are performing separate source detection on images smoothed by two different smoothing lengths, SExtractor often identifies multiple nearby detections associated with the same source. If these were left in our seed catalog, they would lead to over-deblending at the deblending stage (i.e., the source flux would be erroneously deblended into these multiple detections). To account for this, for each seed detection we identify all other seed detections within a $30''$ radius (the radius of the aperture used for photometry measurements) and retain the detection with the lowest P_{False} in our $20''$-smoothed maps (even if initially detected in the $10''$-smoothed maps). Again, this is done to increase the likelihood that a detection in our seed catalog will ultimately satisfy our final significance cut.

We take a similar approach to match sources identified in our three different energy bands. For each detection in the 3–24 keV band, we identify the nearest source within a $30''$ search radius in the other two energy bands, resulting in up to three different positions (i.e., one position for each band). Our final position is taken from the band giving the lowest P_{False} (based on a $20''$ radius smoothing) to again maximize the likelihood that it will pass our final significance cut. All further analyses (i.e., aperture photometry, deblending) are performed using this final position.

After combining the seed catalogs from the three separate bands, we apply our more conservative P_{False} cuts. For this, we calculate the seed source P_{False} in each band based on a $20''$ extraction radius (irrespective of whether the source was detected at $10''$ or $20''$ radius smoothing), and remove those that do not meet our final cuts ($\log(P_{False}) \leqslant -5.19$, $\leqslant -5.22$, and $\leqslant -5.34$ in the 3–8, 8–24, and 3–24 keV bands, respectively). We also remove any sources in areas of low exposure ($< 4 \times 10^4$ s, corresponding to $\lesssim 10\%$ of the peak vignetted survey exposure).

In total, the above procedure returned 54 sources detected in at least one band that constitute our final source catalog. Aperture photometry was performed at the positions of these significant, detected sources followed by deblending, as described in the following subsection.

2.3.2. Net Counts and Deblending

We derive net counts, count rates, and fluxes at the positions of all of the significantly detected sources identified using the procedure described above. To determine total (i.e., source + background) counts for our detections, we summed the total number of counts within $30''$ of the final source position in the combined (i.e., FPMA+FPMB) science mosaics. This aperture size was chosen as a compromise between attempting to maintain as low an aperture correction as possible (a factor of 2.24 for $30''$) and reducing the level of contamination from neighboring sources. Furthermore, tests showed that, compared to using $15''$ and $45''$ apertures, $30''$ led to *NuSTAR* 3–8 keV fluxes that most closely matched those derived from *Chandra* observations (see Sections 2.3.3 and 2.3.4). Total background-only counts were calculated in the same sized apertures centered on the positions of our detected seeds using the background images described in Section 2.2.2. The net number

of counts for each detection was calculated by subtracting the background counts from the total counts. The upper and lower 1σ confidence limits on the total source counts are calculated following Gehrels (1986). To this we add the background error ($\sigma_{\rm Bgd}$) in quadrature with the source count error to derive the error on the net count rate, scaling the background counts by a factor of 125, which is roughly the ratio between the area of the $30''$ aperture used for photometry measurements and the total area over which the background model is defined (i.e., $= 4 \times 5' \times 5'$):

$$\sigma_{\rm Bgd} = \left(1 + \sqrt{125 C_{\rm Bgd} + 0.75}\right)\Big/125, \qquad (2)$$

where $C_{\rm Bgd}$ is the total number of background counts extracted from the background image described in Section 2.2.2.

The relatively extended point-spread function (PSF) of *NuSTAR* means we must factor in the contribution from neighboring detections to the measured count rates and fluxes. To deblend a given detection in our final catalog, we assume that the net photon counts within the adopted $30''$ radius aperture are the sum of that due to that detected source plus the contribution from any other *NuSTAR*-detected sources within $90''$ (all of the sources in the ECDFS are faint enough for any contribution from sources outside this radius to be considered negligible). Although we acknowledge that there will also be some contribution from *NuSTAR*-undetected sources, our goal here is to produce a catalog based solely on *NuSTAR* data, rather than relying on prior (e.g., *Chandra* or *XMM-Newton*) information. We make the simplifying assumption that the contribution of a neighboring source is a function of only its brightness and separation from the source of interest. Under this assumption, the problem of deblending reduces to a set of solvable linear simultaneous equations; for example, in the case of three sources, they are

$$C_{\rm T}^1 = N(r_{1,1})C_{\rm D}^1 + N(r_{1,2})C_{\rm D}^2 + N(r_{1,3})C_{\rm D}^3$$
$$C_{\rm T}^2 = N(r_{2,1})C_{\rm D}^1 + N(r_{2,2})C_{\rm D}^2 + N(r_{2,3})C_{\rm D}^3$$
$$C_{\rm T}^3 = N(r_{3,1})C_{\rm D}^1 + N(r_{3,2})C_{\rm D}^2 + N(r_{3,3})C_{\rm D}^3, \qquad (3)$$

where $C_{\rm T}^n$ is the total net photon counts within the $30''$ aperture of source n, $C_{\rm D}^n$ is the deblended net photon count of source n (again, within $30''$), and $N(r_{n,m})$ is the relative normalization that takes into account the separation between the sources n and m (normalized to one at $N(r_{n,n} = 0)$). In reality, this is complicated by the nonazimuthally symmetric PSF that lengthens with increasing off-axis angle. From simulations, we estimate that the effect of this on the deblended flux of our detected sources is small compared to photometric uncertainties, i.e., typically $\sim$8%. Positional uncertainties are not taken into account in calculating the uncertainties on deblended count rates, but uncertainties in $C_{\rm T}$ are factored in using a Monte Carlo technique, whereby Gaussian noise (appropriate for the high net counts of our significantly detected sources) is added to each $C_{\rm T}$ according to the uncertainty on this value. This is performed 10^4 times for each source, and the resulting distribution (which is closely approximated with a Gaussian due to regression to the mean) for $C_{\rm D}$ is assumed to give the uncertainty on this value.

At this stage we also perform deblending assuming a $20''$-radius aperture (compared to the $30''$ used above for aperture photometry); recall that initial source detection is performed using both $10''$ and $20''$ radius smoothing (see Section 2.3.1). We then use these $20''$ deblended counts, in conjunction with the background photon counts, to recalculate the $P_{\rm False}$ of each source post-deblending and flag (but not remove) those that are no longer significant after deblending. Of the 54 sources in the final catalog, five are flagged as being no longer significant post-deblending, leaving 49 sources that are significant post-deblending.

From the deblended $30''$-aperture net photon counts, we calculate net count rates (and associated uncertainties) using the mean combined (i.e., the sum of both detectors) effective exposure time within a $30''$ aperture of the detected seed position. Deblended 8–24 to 3–8 keV band ratios are calculated using the Bayesian estimation of hardness ratios (BEHR) method described in Park et al. (2006).[37] We report the median and upper and lower 68th percentiles (i.e., 1σ uncertainties) returned by this method. Photon indices and fluxes were calculated from these deblended band ratios and net count rates following the procedure described in the next subsection.

2.3.3. Flux Calculation

Following the same basic approach as Alexander et al. (2013), observed deblended fluxes in each band and effective photon indices (i.e., Γ) were calculated from the deblended $30''$ aperture count rates using conversion factors derived from XSPEC model spectra. To generate the conversion factors, we use XSPEC's `fakeit` command to model power-law spectra spanning a range of power-law indices ($0.0 < \Gamma < 3.0$, in increments of 0.01; XSPEC model: `pow`) and taking the rmf and arf at the aim point of the two detectors into account. "Fake" fluxes and count rates in the three bands were extracted from these synthetic spectra and were used to generate polynomial solutions that relate observed fluxes and photon indices to our observed count rates and 8–24 to 3–8 keV band ratios:

$$\frac{f_{\rm E}}{R_{\rm E}} = 10^{-14} \sum_{i=0}^{n} a_i \Gamma^i, \qquad (4)$$

where

$$\Gamma = \sum_{i=0}^{n} a_i b^i \qquad (5)$$

and $f_{\rm E}$ is the flux within a given energy band (in erg s^{-1} cm^{-2}), $R_{\rm E}$ is the count rate in the same energy band (in ks^{-1}), $b = \log\left(R_{8-24\,{\rm keV}}/R_{3-8\,{\rm keV}}\right)$ (i.e., the logarithm of the 8–24 to 3–8 keV band ratio), and Γ is the observed (i.e., not corrected for absorption) photon index. The polynomial coefficients for the above equations, a_i, are given in Table 2 and reproduce the XSPEC fluxes and photon indices to within 1% across $-0.7 < b < 0.4$ (corresponding to $0.0 < \Gamma < 3.0$). Where a source is detected in both the 3–8 and 8–24 keV bands (and thus has a well-constrained photon index), we use the derived photon index; otherwise we assume a fixed Γ of 1.8 (corresponding to count rate to flux conversions of 7.2×10^{-14}, 1.5×10^{-13}, and 1.0×10^{-13} erg s^{-1} cm^{-2} ks for the 3–8, 8–24, and 3–24 keV bands, respectively). These flux conversions take the size of the aperture into account to

---

[37] BEHR code available from http://hea-www.harvard.edu/astrostat/behr/

Table 2
Polynomial Coefficients for Calculating Fluxes and Γ

(1) Property	(2) a_0	(3) a_1	(4) a_2	(5) a_3	(6) a_4
f_{SB}	6.38	0.78	−0.32	0.10	−0.01
f_{HB}	21.01	−3.12	−0.27	0.19	−0.02
f_{FB}	17.13	−4.38	−0.21	0.42	−0.06
Γ	1.27	−2.81	0.04	−0.06	−0.12

Note. (1): f_{SB}, f_{HB}, and f_{FB} correspond to the aperture-corrected fluxes in the 3–8, 8–24, and 3–24 keV bands, respectively, in 10^{-14} erg s^{-1} cm^{-2}. (2)–(6): The polynomial coefficients used with Equations (4) and (5).

return aperture-corrected fluxes (which are reported throughout).

To verify the accuracy of our process for calculating deblended *NuSTAR* fluxes, we carry out a comparison between the *NuSTAR*-derived 3–8 keV fluxes and the total *Chandra*-derived 3–8 keV fluxes arising from all *Chandra* sources within 30″ of the *NuSTAR* source position combined. This comparison is shown in Figure 5. The *NuSTAR* fluxes cluster along the 1:1 line shown on this plot, and all but two *NuSTAR* sources are consistent (within 3σ errors) with the total *Chandra* flux to within a factor of two, thereby validating our approach of calculating *NuSTAR* fluxes. We note that some of the scatter in this plot is expected to be introduced by intrinsic source variability (e.g., Paolillo et al. 2004; Young et al. 2012) and spurious matches between the *NuSTAR* and *Chandra* sources (see Section 2.3.4).

We can calculate the limiting flux at every point in the final mosaics using the background and exposure maps, assuming the detection P_{False} thresholds introduced in Section 2.3.1 (i.e., $\log(P_{False}) \leqslant -5.19$, $\leqslant -5.22$ and $\leqslant -5.34$ in the 3–8, 8–24, and 3–24 keV bands, respectively), and using the count rate to flux conversions above, assuming $\Gamma = 1.8$. We use this to determine the area of the survey reaching a given flux limit in each of our bands, the results of which are shown in Figure 6. The most sensitive regions of the survey reach $\approx 1.3 \times 10^{-14}$, $\approx 3.4 \times 10^{-14}$, and $\approx 3.0 \times 10^{-14}$ erg s^{-1} cm^{-2} in the 3–8, 8–24, and 3–24 keV bands, respectively. We note, however, that these are the theoretical flux limits of the survey for isolated sources. In reality, the relatively large *NuSTAR* PSF may affect the total area to a given limit because regions around bright sources are less sensitive due to contamination and issues arising from deblending. A full understanding of these second-order factors will be necessary to obtain, for example, source number counts and luminosity functions, to be published in F. Harrison et al. (2015, in preparation) and J. Aird et al. (2015, in preparation).

2.3.4. Multiwavelength Counterparts, Redshifts, and Luminosity Determination

A major benefit of observing the ECDFS with *NuSTAR* is the wealth of ancillary multiwavelength data available for the field, making the characterization of identified sources comparatively straightforward. Because much of these ancillary data have already been matched to sources identified in the *Chandra* and *XMM-Newton* observations of this field (i.e., the *Chandra* 250 ks ECDFS, *Chandra* 4 Ms CDFS, and *XMM-Newton* 3 Ms ECDFS surveys; described in L05, Xue et al.
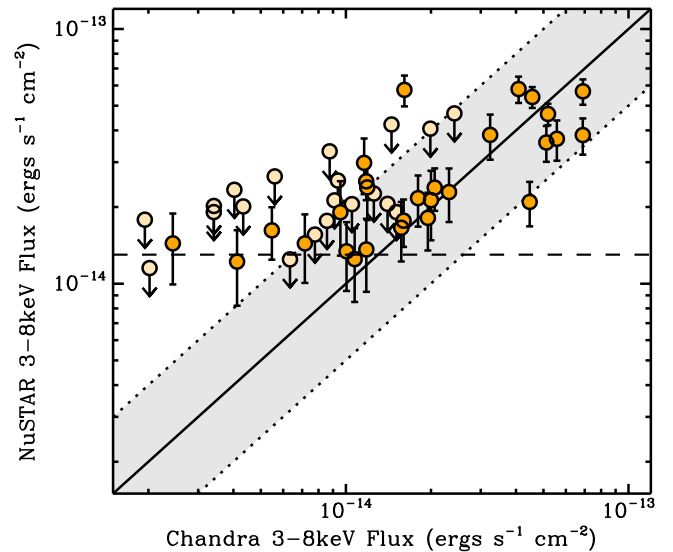

Figure 5. Comparison of deblended, aperture-corrected *NuSTAR* 3–8 keV fluxes versus the *Chandra*-measured fluxes of all the *Chandra* sources within 30″ of the *NuSTAR* source position. Filled circles represent 3σ detections, and open circles represent 3σ upper limits. The solid line shows the 1:1 relation, and the gray shading indicates the region within a factor of three of this line. The dashed horizontal line indicates the sensitivity limit of the deepest region of the survey in the 3–8 keV band, i.e., $\approx 1.3 \times 10^{-14}$ erg s^{-1} cm^{-2}.
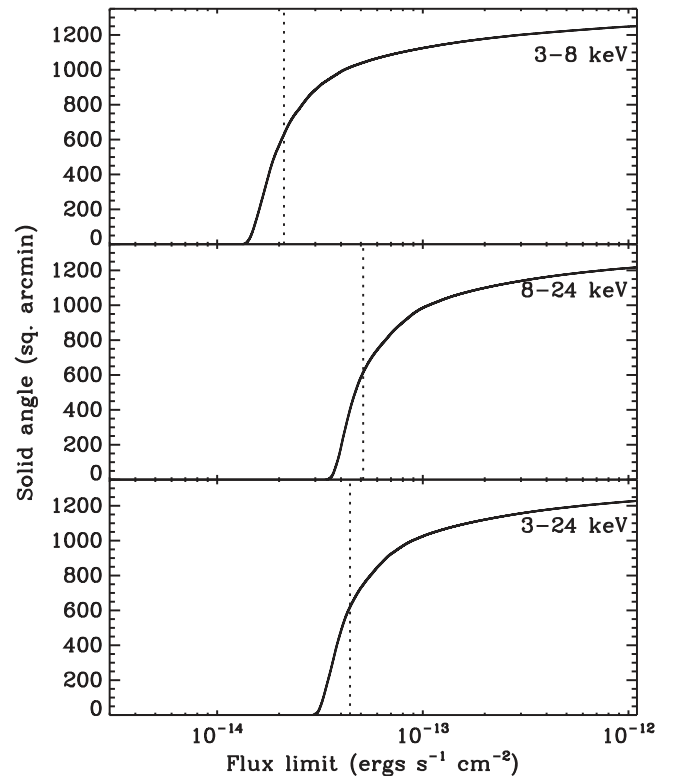

Figure 6. Plot showing the solid angle of the survey below a given aperture-corrected flux sensitivity (shown on the abscissa) corresponding to an S/N of three in each of our *NuSTAR* bands. These sensitivity limits were calculated from the background and exposure mosaics alone using the procedure outlined in Section 2.3.3. The most sensitive regions in the 3–8, 8–24, and 3–24 keV bands reach $\approx 1.3 \times 10^{-14}$, $\approx 3.4 \times 10^{-14}$, and $\approx 3.0 \times 10^{-14}$ erg s^{-1} cm^{-2}. The dotted lines indicate the flux limits for an area of ≈ 630 arcmin^2, which is roughly half the solid angle of the full *NuSTAR* ECDFS survey, and corresponds to values of $\approx 2.1 \times 10^{-14}$, $\approx 5.1 \times 10^{-14}$, and $\approx 4.4 \times 10^{-14}$ erg s^{-1} cm^{-2} for the 3–8, 8–24, and 3–24 keV bands, respectively.

2011, Ranalli et al. 2013, respectively), we obtain this information by matching to these previous X-ray catalogs. We first match to the *Chandra*-250 ks ECDFS catalog (L05) using a $30''$ search radius. We report all matches that contribute at least 20% of the total flux from all *Chandra* sources within $30''$ of the *NuSTAR* position (i.e., we ignore those faint *Chandra* sources that do not contribute significantly to the total *Chandra* flux within the search radius). Following this prescription, of the 54 sources in our final catalog, 48 were found to have at least one *Chandra* counterpart within the search radius. Of these, twelve *NuSTAR* sources were found to have two *Chandra* matches. No *NuSTAR* source was found to have more than two *Chandra* matches within the search radius. Of the 49 *NuSTAR* sources that are significant post-deblending, 44 have at least one *Chandra* counterpart.

Considering all 809 *Chandra* sources listed in L05 with our $30''$ matching radius corresponds to a high spurious matching fraction of ∼70% for our sample. However, we note that the majority (∼85%) of matched *Chandra* counterparts have *Chandra* 3–8 keV fluxes $>2 \times 10^{-15}$ erg s^{-1} cm^{-2}, of which there are 289 in the full L05 catalog. Considering only these sources corresponds to a spurious matching fraction of ∼25%, which we consider to be a more reasonable estimation for the spurious matching fraction for our sample. Of course, following this logic, brighter *Chandra* counterparts are less likely to be spurious than fainter sources; we estimate the spurious matching fraction of $F_{3-8\,\mathrm{keV}} > 10^{-14}$ erg s^{-1} cm^{-2} *Chandra* sources to be ∼3%, compared to ∼40% for $F_{3-8\,\mathrm{keV}} > 10^{-15}$ erg s^{-1} cm^{-2}.

The six (of 54) sources without *Chandra* 250 ks counterparts were then matched against the *Chandra*-4 Ms CDFS catalog (again, using a $30''$ search radius), which led to two further matches (and no multiple matches). Finally, the remaining four *NuSTAR* sources without counterparts were matched against the *XMM-Newton* 3 Ms catalog, which resulted in one further match. As a result, only three *NuSTAR* sources have no *Chandra* or *XMM-Newton* counterpart, all three of which are significant post-deblending.

Where a *Chandra* or *XMM-Newton* counterpart is identified, the associated optical counterpart is taken from the respective catalog (i.e., L05, Xue et al. 2011, or Ranalli et al. 2013 for *Chandra* ECDFS, CDFS, and *XMM-Newton*-ECDFS, respectively), together with its associated redshift, if available. We adopt the spectroscopic redshift in preference to the photometric redshift in cases where both are available. Of the 51 sources for which there are either *Chandra* or *XMM-Newton* counterparts, 46 have spectroscopic redshifts and three have only photometric redshifts (i.e., giving 49 in total). The corresponding numbers for those 49 sources that are significant post-deblending are 41 with spectroscopic redshifts and three with photometric redshifts (i.e., 44 in total).

For those sources for which either spectroscopic or photometric redshifts are available, rest-frame 10–40 keV (non-absorption-corrected) luminosities were calculated from the 8–24 keV fluxes. The *k-corrections* were performed by adopting the derived photon index for sources that were significantly detected in both the 3–8 and 8–24 keV bands; otherwise $\Gamma = 1.8$ is assumed. In this work, we do not attempt to correct the luminosities for the effects of absorption; this will be the focus of a later study to combine *Chandra* and/or *XMM-Newton* data with the *NuSTAR* data to obtain the most reliable absorbing column densities (and hence, corrected luminosities)

currently achievable (A. Del Moro et al. 2015 in preparation; L. Zappacosta et al. 2015, in preparation).

3. RESULTS

In this section, we describe the properties of the detected sources and compare them against local ($z < 0.3$) hard X-ray sources detected in the *Swift*-BAT survey and those in the *NuSTAR* serendipitous survey (Alexander et al. 2013). We also highlight three *NuSTAR* sources that are undetected in both the *Chandra* and *XMM-Newton* coverage of the ECDFS and CDFS and that may therefore represent previously unknown contributors to the hard X-ray background.

3.1. Basic Properties

As reported in Section 2.3.1, our final catalog contains 54 sources that are initially detected as significant in at least one of the three standard bands. However, of these 54, five are not significant after the effects of neighboring sources have been taken into account (i.e., after deblending). While these five are retained in the electronic catalog, the results described in the remainder of this paper consider only the 49 sources that are significant post-deblending.

It should also be noted that, since source detection is separate from photometry, some of our significantly detected sources (i.e., nine) have $<3\sigma$ counts in all three bands. Because they pass our formal P_{False} threshold, these sources are retained in the electronic catalog and are considered in our general analyses and histograms, but are shown as 3σ upper limits in Cartesian plots.

Of the 49 sources that make up our final, post-deblended catalog, 12 are significant (i.e., satisfy the P_{False} cuts outlined in Section 2.3.1) in all three bands, 16 in exactly two (13 in 3–8 keV+3–24 keV, three in 8–24 keV+3–24 keV), and eight, four, and nine in the 3–8, 8–24, and 3–24 keV bands only, respectively. As such, 19 are detected in the 8–24 keV band, the photon energy range probed to unique depths by *NuSTAR*. We compare these numbers of detected sources to those predicted by the X-ray background synthesis model described in Ballantyne et al. (2011), updated to the Ueda et al. (2014) luminosity function and using an AGN spectrum closely following that described in Ballantyne (2014), which assumes $\langle \Gamma \rangle = 1.85$ and a Burlon et al. (2011) N_{H} distribution. Convolving this model with the *NuSTAR* ECDFS sensitivity curve predicts ≈25, ≈13, and ≈28 sources in the 3–8, 8–24, and 3–24 keV bands, respectively. With 33, 19, and 37 detected sources in the 3–8, 8–24, and 3–24 keV bands, respectively, this model underpredicts the actual number of detected sources by a modest amount, ≈25%–30%. Interestingly, the biggest percentage difference between the number of predicted and detected sources is at 8–24 keV, possibly suggesting a deviation from the adopted model AGN spectrum at these newly probed energies, although we note that this comparison will be affected by the small numbers of our sample and field-to-field variations.

The distributions of source count rates in each of our bands are plotted in Figure 7. Here, we include all 49 significant sources, irrespective of their S/Ns, based on our $30''$ photometry measurement. The number of significant sources peaks at ∼0.2, ∼0.1, and ∼0.3 ks^{-1} in the 3–8, 8–24, and 3–24 keV bands, respectively. The lowest number of deblended net source counts in each band are 38, 37, and 36 in
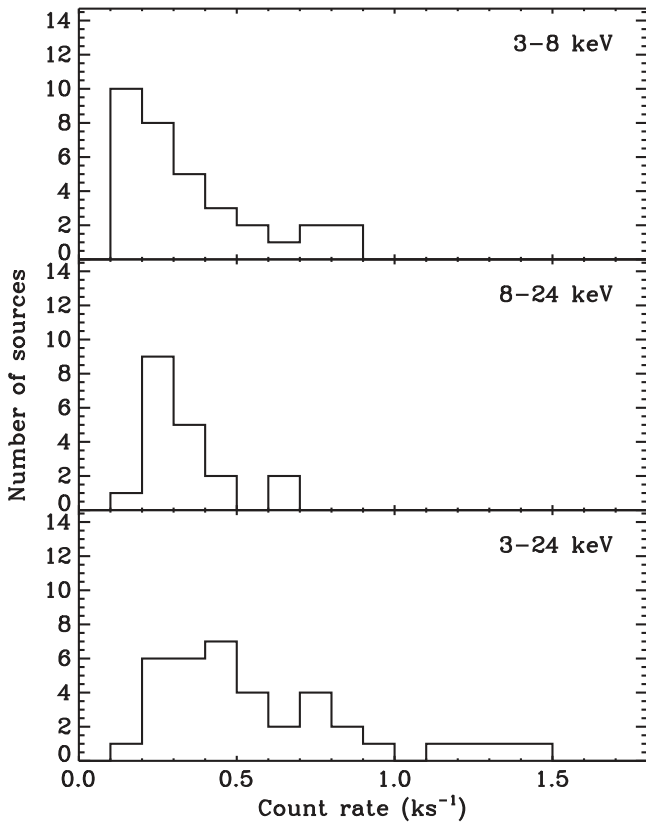
Figure 7. Distributions of non-aperture-corrected count rates in our three bands for the sources in the "blind" catalog. Here, we only include the 49 sources that pass our significance cuts post-deblending.

Figure 8. The 8–24 to 3–8 keV band ratio (bottom axis) and Γ (top axis) distributions for our sample of "blind" sources. The solid lines indicate the distribution of sources that pass our significance threshold in both bands after deblending. The gray-shaded histograms show the distribution resulting from a Monte Carlo analysis of all 49 sources that pass our significance cut in at least one band after deblending, incorporating the uncertainties on the individual band ratios and photon indices (see Section 3.1).

Figure 9. The 8–24 to 3–8 keV band ratio plotted against the aperture-corrected 3–24 keV band count rates of our detected sources. The average band ratios in three separate bins of 3–24 keV band count rate, calculated by summing the counts from *all* sources in each bin to obtain a stacked detection in each band, are shown as red stars. Horizontal dotted lines indicate the photon index at various band ratios.

the 3–8, 8–24, and 3–24 keV bands, respectively, and correspond to two separate sources (NuSTAR J033121−2757.8 [source ID 2 in our table] has the lowest number of counts in the 3–8 keV band, whereas NuSTAR J033144−2803.0 [ID: 8] has the lowest number of counts in both the 8–24 and 3–24 keV bands). Conversely, the highest net source counts in each band are 365, 197, and 545, respectively, and do correspond to the same source (NuSTAR J530642−2741.0 [ID: 29]).

Figure 8 shows the distribution of 8–24 to 3–8 keV band ratios for all sources that pass our significance threshold (post-deblending) in both the 8–24 and 3–8 keV bands. Shown on the top axis of this plot is the corresponding Γ value. Because the range of band ratios is sparsely sampled, it is difficult to interpret from the significant sources alone where the band ratio distribution of our detected sources peaks. Further insight into the distribution of band ratios for all of our detected sources can be gained by taking a Monte Carlo approach to account for uncertainties in their count rates. We generate 10^4 mock band ratios for each detection by randomly sampling the band ratio probability density profiles output by the BEHR code. The resulting band ratio distribution is shown in gray in Figure 8 behind the histogram of those sources significantly detected in both bands, and it peaks at ∼0.5, corresponding to $\Gamma \sim 2.1$. We stress that this distribution only samples the detected sources and may not be representative of the underlying band ratio distribution of the entire AGN population, which may be probed using more advanced techniques that are beyond the scope of this work (e.g., stacking on the positions of known AGN populations from, e.g., *Chandra* observations).
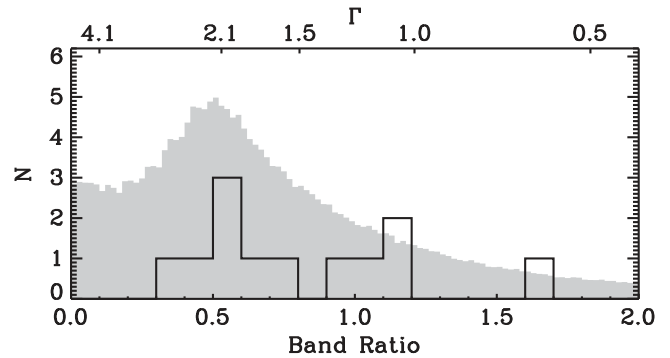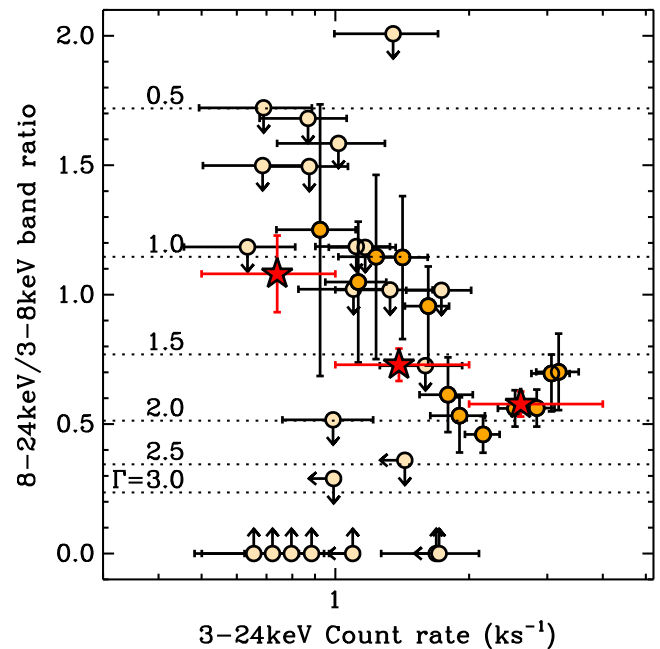
Previous studies of deep X-ray surveys have reported an anticorrelation between the band ratio and count rate in the lower energy bands (i.e., 2–8 to 0.5–2 keV versus 0.5–8 keV count rates) for AGN-dominated sources (e.g., della Ceca et al. 1999; Ueda et al. 1999; Mushotzky et al. 2000; Tozzi et al. 2001; Alexander et al. 2003). This trend has been attributed to an increase in the number of absorbed AGNs detected at lower count rates. To investigate whether we see such a trend in the *NuSTAR* data, we plot the 8–24 to 3–8 keV band ratio as a function of 3–24 keV count rate in Figure 9. The 12 sources that are detected at $>3\sigma$ in both the 8–24 and 3–8 keV bands appear to show a weak trend toward higher band ratios at low 3–24 keV count rates. However, the large number of sources with upper limits in either band and the

narrow dynamical range in 3–24 keV count rates of those sources detected in all three bands make it difficult to assess the significance of this trend. To investigate this possible trend, we determine average count rates in three 3–24 keV count rate bins, i.e., $0.5 \leqslant R_{FB}/ks^{-1} < 1$, $1 \leqslant R_{FB}/ks^{-1} < 2$, and $2 \leqslant R_{FB}/ks^{-1} < 4$, getting $>3\sigma$ average count rates for all bands in each bin. The result of this averaging is shown in Figure 9 and shows some evidence of a decreasing hardness ratio with increasing 3–24 keV count rate, supporting previous claims from studies of lower energy X-ray bands. However, we stress that this new result is only based on three count-rate bins, and confirmation will be needed by extending the dynamical range in average count rates by, for example, stacking the *NuSTAR*-undetected population, which will be the focus of a future study (e.g., C. Hickox et al. 2015, in preparation).

In the electronic catalog, we also provide derived properties for each of our detected sources, namely the photon index, Γ, and the observed flux in each band (i.e., not corrected for absorption). The 12 sources that pass our significance thresholds in both the 8–24 and 3–8 keV bands cover a wide range of observed (uncorrected) photon indices, ranging from $0.51^{+0.89}_{-0.24}$ to $2.27^{+0.47}_{-0.37}$ (1σ errors; see Figure 8). The majority (seven of 12) of sources in our sample for which we can constrain a photon index have $\Gamma < 1.8$ (i.e., the typically assumed intrinsic AGN photon index), suggesting that a large fraction of the sources have significant obscuration, causing the observed photon index to harden. The median photon index and $\pm 1\sigma$ interval for these 12 sources is $\overline{\Gamma} = 1.70 \pm 0.52$. We use the same Monte Carlo simulations as described earlier in this section (i.e., those used to incorporate uncertainties in the band ratio distribution) to calculate the median photon index for all sources, including those not individually detected in both bands, finding a somewhat softer $\overline{\Gamma} = 1.90 \pm 0.53$.

In Figure 10 we plot the distribution of fluxes of our detected sources in each of the three bands. The faintest sources in the 3–8, 8–24, and 3–24 keV bands have fluxes of $(8.3 \pm 3.6) \times 10^{-15}$, $(2.2 \pm 1.3) \times 10^{-14}$, and $(1.59 \pm 0.84) \times 10^{-14}$ erg s^{-1} cm^{-2}, respectively, giving an indication of the approximate ultimate sensitivity limit of the survey in these bands. However, while passing our significance thresholds, these sources all have flux measurements below 3σ. The faintest sources with $>3\sigma$ flux measurements have fluxes of $(1.22 \pm 0.40) \times 10^{-15}$, $(3.4 \pm 1.1) \times 10^{-14}$, and $(2.36 \pm 0.74) \times 10^{-14}$ erg s^{-1} cm^{-2} in the 3–8, 8–24, and 3–24 keV bands, respectively. The 8–24 and 3–24 keV band flux limits are roughly two orders of magnitude fainter than those of the most sensitive observations of the *Swift*-BAT all-sky survey (Baumgartner et al. 2013), the previous deepest hard X-ray survey prior to the launch of *NuSTAR*. We note that the flux limit of the ECDFS survey is comparable to that of the six deepest observations that make up the *NuSTAR* Serendipitous survey (Alexander et al. 2013), although the ECDFS survey reaches this depth over a larger contiguous area and benefits from more comprehensive ancillary multiwavelength data, an aspect that is exploited in the next subsection.

The 44 sources in our sample with known redshifts span the redshift range $z = 0.22$–2.7 (see Figure 11). The 10–40 keV luminosity range of the 19 of these 44 that are significantly detected in the 8–24 keV band (from which we calculated 10–40 keV luminosities) spans the range $\sim 8 \times 10^{42}$ to $\sim 3 \times 10^{45}$ erg s^{-1}. The redshift–luminosity plane for our
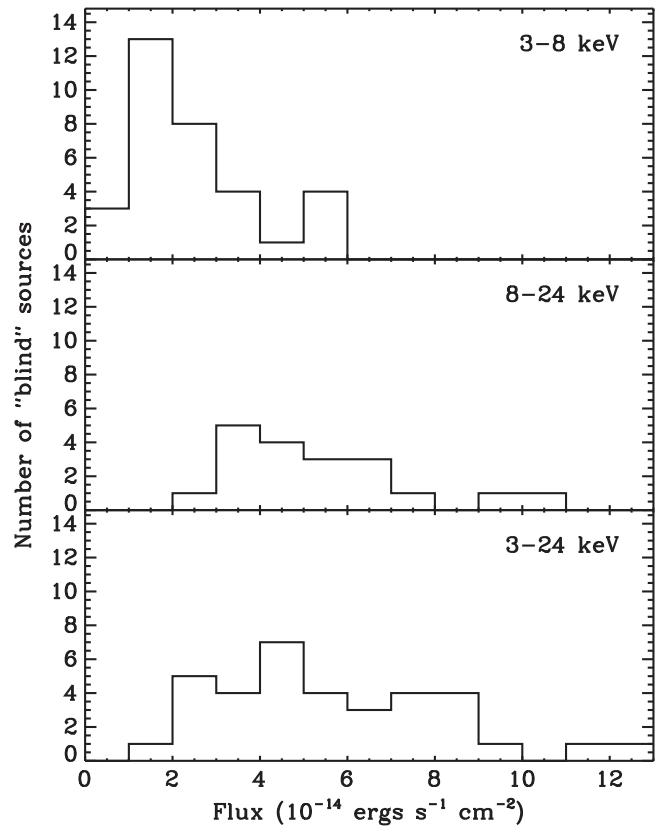

Figure 10. Distributions of aperture-corrected fluxes in our three bands for the sources in the "blind" catalog. Here, we only include the 49 sources that pass our significance threshold post-deblending.
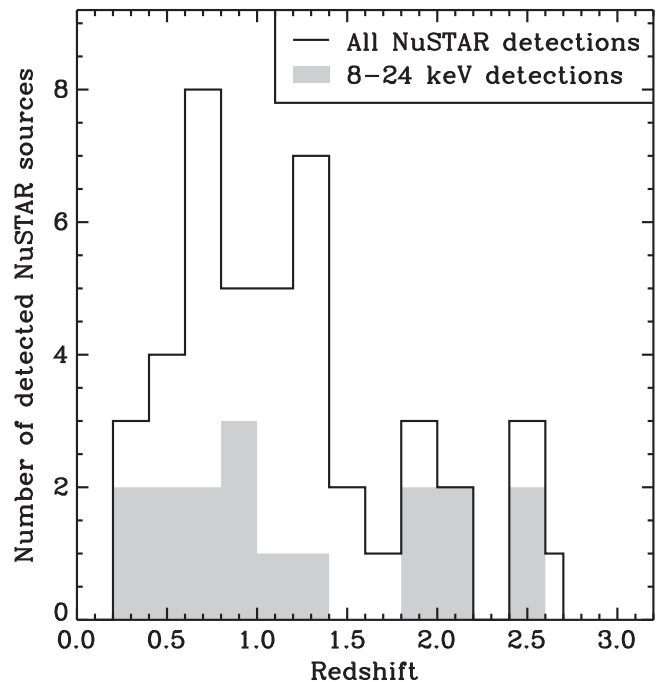

Figure 11. Redshift distribution of the 44 *NuSTAR* sources that are significantly detected (post-deblending) in at least one band and have either an associated spectroscopic or photometric redshift (solid line). The shaded histogram shows the same for the 17 sources significantly detected (post-deblending) in the 8–24 keV band that have either a spectroscopic or photometric redshift.
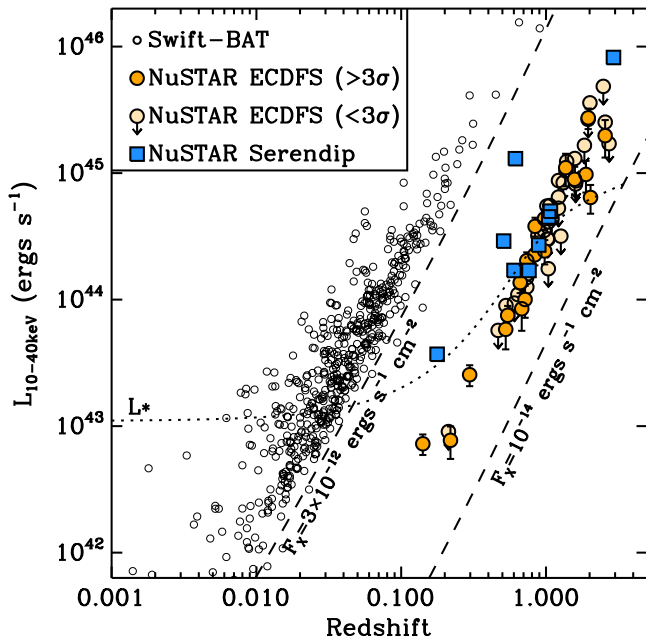
Figure 12. X-ray luminosity in the rest-frame 10–40 keV band versus redshift for several hard X-ray selected samples. We show the NuSTAR-ECDFS sources (our sample), the first 10 sources from the *NuSTAR* serendipitous survey (Alexander et al. 2013), and the sources from the *Swift*-BAT survey (Baumgartner et al. 2013). In the case of the NuSTAR-ECDFS sources, the 10–40 keV luminosity is derived from the observed 8–24 keV flux, assuming either the measured photon index (Γ), if the source is significantly detected in both the 3–8 and 8–24 keV bands, or $\Gamma = 1.8$ otherwise. Upper limits are shown for NuSTAR-ECDFS sources when the measured flux in the 8–24 keV band is $<3\sigma$. The dotted line indicates the evolution of the position of the knee of the X-ray luminosity function, extrapolated from the 2–10 keV luminosity functions of Aird et al. (2010) assuming $\Gamma = 1.8$. The *NuSTAR* sources in the ECDFS probe to this "knee" out to $z \sim 1$.

sample, together with comparison samples from the *Swift*-BAT survey (Baumgartner et al. 2013) and the *NuSTAR* serendipitous survey (Alexander et al. 2013), is shown in Figure 12 and highlights the complementary regions of parameter space that these various surveys cover, which is the focus of the following subsection.

3.2. Comparison with Low-z Samples

The AGNs detected and characterized as part of the all-sky *Swift*-BAT survey form the local sample that is most directly comparable to the *NuSTAR*-ECDFS AGNs reported here. Figure 12 shows that, while the range in luminosities of both samples is large (i.e., each spanning roughly three orders of magnitude or more) and there is some overlap, the AGNs in the ECDFS survey are typically an order of magnitude more luminous than those in the *Swift*-BAT sample. As expected, the difference in the redshift distributions of the two samples is also large, with the ECDFS sample centered around $z \sim 1$, compared to $z \sim 0.03$ for the *Swift*-BAT sample.

To help place the two samples in a cosmological context, we include a line in Figure 12 showing the evolution in the position of the knee (i.e., L^*) of the AGN luminosity function (converted to 10–40 keV from the 2–10 keV luminosity functions of Aird et al. 2010 assuming an intrinsic photon index of $\Gamma = 1.8$). The position of the two samples relative to this line demonstrates the complementary nature of these samples, with the *Swift*-BAT sample probing the knee of the luminosity function at $z \sim 0.015$ and the ECDFS sample probing it at

$z \sim 0.8-1$. Crucially, this means that, because of the evolution of the SMBH accretion rate density, the power of *NuSTAR* and *Swift*-BAT combined will enable us to probe roughly 25% of the accretion rate density of the universe with hard X-rays, compared to just 0.5% with *Swift*-BAT alone.[38]

4. NUSTAR SOURCES WITHOUT CHANDRA OR XMM-NEWTON COUNTERPARTS

One of *NuSTAR*'s primary scientific goals is the characterization of the sources that make up the hard (>10 keV) X-ray background. As such, any sources that have not previously been identified at softer X-ray energies are potentially of great interest. In this subsection, we focus on the three *NuSTAR* sources in the ECDFS field that we have identified as having neither *Chandra* nor *XMM-Newton* counterparts. By the definition of our detection threshold, we should expect, on average, one false source per band. As such, it is plausible that all three of these *NuSTAR* sources with neither *Chandra* nor *XMM-Newton* counterparts are spurious. That said, it is important that we first determine whether any of these three shows any other evidence of nuclear activity before rejecting them as spurious because, if confirmed, they may provide further insight into the population of Compton-thick AGNs at high redshift.

The three *NuSTAR* sources without *Chandra* or *XMM-Newton* counterparts are NuSTAR J033122–2743.9, NuSTAR J033228–2803.5, and NuSTAR J033231–2737.3 (hereafter referred to by their indices in our source catalog, 3, 31, and 37, respectively). These three sources represent $\sim6\%$ of the total sample of the 49 *NuSTAR* sources that are significant post-deblending. We checked by eye the (5 and 10 pixels Gaussian-smoothed) 2–8 keV *Chandra* images of the ECDFS near the positions of these three *NuSTAR* sources, but find no indication of any weak sources that may have been missed by the source detection algorithm used in analyzing the *Chandra* data (see L05). We note that two of the three sources are significantly detected in only one of our three *NuSTAR* bands: one in the 8–24 keV band (ID: 3) and one in the 3–24 keV band (ID: 31). The third (ID: 37) is detected in both the 3–8 and 3–24 keV bands. Furthermore, two of these sources have $>3\sigma$ deblended fluxes in at least one band (which coincides with the band in which it is significantly detected), the exception being ID 37. Due to their faintness, all but one of these three new X-ray sources have poorly constrained photon indices, the exception being ID: 31, for which BEHR gives a (median) band ratio of $0.87^{+0.38}_{-0.45}$, corresponding to a photon index of $\Gamma = 1.3^{+1.0}_{-0.3}$.

We next explore whether any of the three new X-ray sources have counterparts displaying signs of nuclear activity at wavelengths aside from X-rays (see Figure 13 for $90'' \times 90''$ postage-stamp images of the regions around the *NuSTAR* sources in the K band, *Spitzer*-IRAC Ch. 4 and MIPS 24 μm bands, and *Herschel*-PACS 100 μm bands). We first consider the near- to mid-infrared regime (specifically *Spitzer*'s IRAC channels) because this has been shown to be efficient at identifying highly obscured AGNs (e.g., Lacy et al. 2004; Stern et al. 2005; Donley et al. 2007, 2012). Furthermore, considering that $\approx94\%$ of *Chandra* sources in the ECDFS have counterparts in at least one of the *Spitzer*-IRAC channels (based on a $3''$ matching to the SIMPLE catalog described in
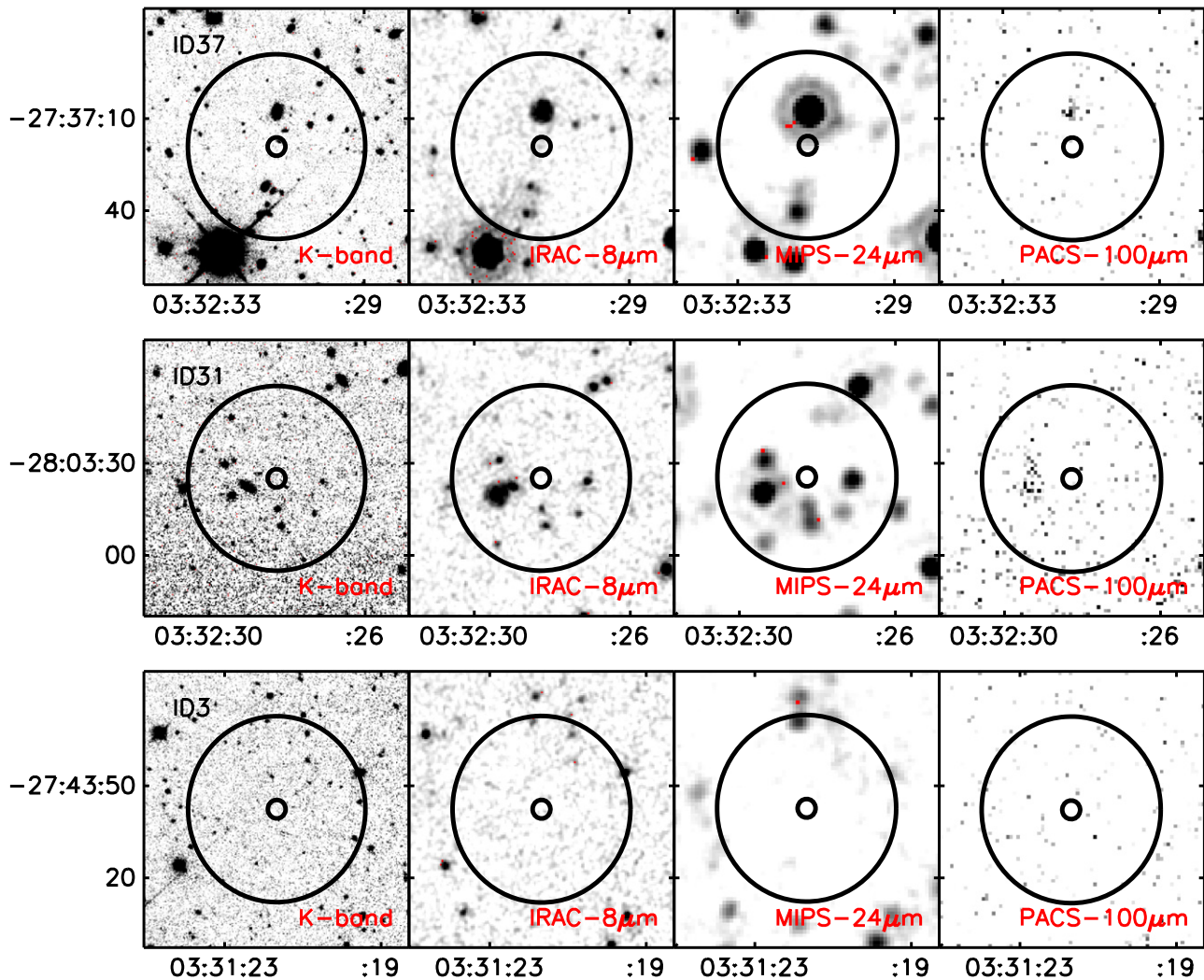

Figure 13. Thumbnail images of the $90'' \times 90''$ patches of sky at various wavelengths centered on the three *NuSTAR* sources without *Chandra* or *XMM-Newton* counterparts. The smaller $3''$-radius circle is used to indicate the location of the *NuSTAR* source, and the larger circle shows the $30''$ search radius we use when identifying counterparts at other wavelengths. The data used to create these images come from TENIS (*K* band; Hsieh et al. 2012), SIMPLE (*Spitzer*-IRAC 8 μm [i.e., Ch. 4]; Damen et al. 2011), FIDEL (*Spitzer*-MIPS 24 μm), and PEP (*Herschel*-PACS; Lutz et al. 2011) surveys. Only one of these, *NuSTAR*-ID: 37, shows any evidence of hosting an AGN at any wavelength other than hard X-rays, which comes from mid- to far-infrared SED fitting (see Figure 14).

Damen et al. 2011), it is highly likely that any genuine *NuSTAR* source will also have a *Spitzer*-IRAC counterpart. Indeed, with an on-sky source density of ∼50 IRAC sources per arcmin^2, the challenge becomes identifying which, if any, of the ∼40 IRAC sources within our $30''$ search radius around the *NuSTAR* positions is the true counterpart (see Figure 13). To address this, we explore whether any of the potential counterparts displays a rising power-law distribution of IRAC fluxes, which is evidence of AGN-heated dust (e.g., Donley et al. 2007, 2012). Considering the IRAC color criteria of Donley et al. (2012), which are optimized for deep IRAC data, unlike the shallow-data criteria of Lacy et al. (2004) and Stern et al. (2005), none of the 95 potential IRAC counterparts show clear evidence of nuclear activity based on IRAC data.

Because IRAC power-law selection will identify only those AGN whose mid-infrared emission strongly dominates that from star formation, we also exploit mid- to far-infrared spectral energy distribution (SED) fitting to identify potential infrared signatures of AGNs. To get broader wavelength coverage for our SED fitting, we match to *Spitzer*-MIPS (i.e., the FIDEL catalog; P.I.: M. Dickinson) and *Herschel*-PACS

data (i.e., the PEP catalog; Lutz et al. 2011; Magnelli et al. 2013), matching the positions of the potential *Spitzer*-IRAC counterparts identified above with a search radius of $3''$. Of the 95 potential IRAC counterparts, only two have detections at 24 μm and at either 100 or 160 μm (our infrared SED fitting requires at least one detection in either of the *Herschel*-PACS bands). The two potential far-infrared counterparts correspond to *NuSTAR* sources 31 and 37 (FIDEL catalog IDs: 1294 and 14000; PEP source names: PEPPRI J033229.3–280329 and PEPPRI J033231.2–273707; and redshifts of $z = 0.204$ and 0.125 from the MUSYC catalog described in Cardamone et al. 2010, respectively), whereas *NuSTAR* source 3 does not have a significant far-infrared counterpart. Following Mullaney et al. (2011), we fit the infrared SEDs of these two potential counterparts using the extended AGN and host galaxy templates of Del Moro et al. (2013). Whereas the counterpart to *NuSTAR* source 31 shows no evidence of an AGN component, the counterpart to *NuSTAR* source 37 requires a significant AGN contribution to fit the infrared SED (required at ≫99% significance; see Figure 14). Furthermore, converting the *NuSTAR* 3–8 keV flux
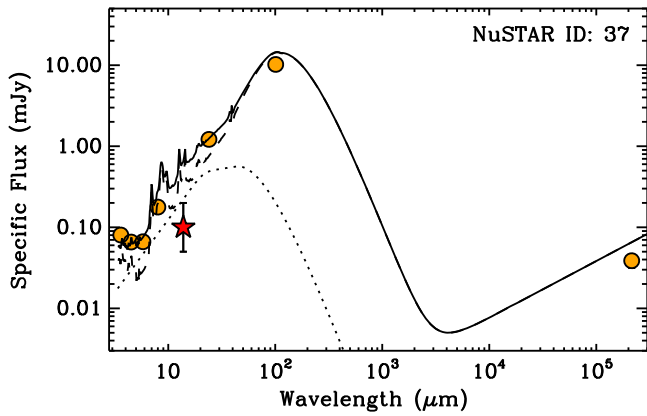
Figure 14. Infrared spectral energy distribution for *NuSTAR*-ID: 37. Orange circles show data from *Spitzer*-IRAC, MIPS, and *Herschel*-PACS and radio data from Bonzini et al. (2012). On fitting the infrared spectral energy distribution of this source using the AGN (dotted line) and host-galaxy (solid line) templates described in Del Moro et al. (2013), we find that an AGN component is required at a significance of ≫99%. The red star shows the mid-infrared flux derived from the *NuSTAR* 3–8 keV flux using Equation (2) of Gandhi et al. (2009), which is broadly consistent with the AGN component required by the SED fit.

to a 2–10 keV luminosity (assuming $\Gamma = 1.8$ and $z = 0.125$) and using Equation (2) from Gandhi et al. (2009) gives a predicted mid-infrared flux broadly consistent with the AGN contribution required by the SED fit, further strengthening the case that this is a genuine AGN. Interestingly, the SED fit also provides an explanation as to why the *Spitzer*-IRAC fluxes do not display a power-law distribution, with Figure 14 showing that the SED is likely dominated by emission from the host galaxy at all infrared wavelengths (e.g., Cardamone et al. 2008).

Finally, following Del Moro et al. (2013), we search for potential radio counterparts to the three *NuSTAR* sources without *Chandra* or *XMM-Newton* matches. Matching to the Bonzini et al. (2012) catalog of radio sources in the ECDFS using a 3″ search radius around the IRAC positions, we find that the two potential far-infrared counterparts identified above are also detected at 1.4 GHz (i.e., matched to *NuSTAR* sources 31 and 37). Because these sources are detected at far-infrared wavelengths, we explore whether either shows a radio excess above that predicted by the far-infrared/radio correlation that could indicate the presence of an obscured AGN. However, we find that the radio fluxes are consistent with star formation in both cases (see Figure 14 for the infrared-to-radio SED of *NuSTAR* ID: 37).

To summarize this section, we detect three *NuSTAR* sources that have neither *Chandra* nor *XMM-Newton* counterparts. From the definition of our detection threshold, we expect two to three of these to be spurious (i.e., due to random noise fluctuations). An analysis of the infrared SEDs of potential counterparts reveals some evidence that one of these *NuSTAR* sources (ID: 37) displays excess flux at mid-infrared wavelengths that may be attributable to an obscured AGN. However, no evidence of this AGN is seen at near-infrared wavelengths (i.e., via power-law *Spitzer*-IRAC fluxes) or radio frequencies (via a radio excess). Further evidence of an obscured AGN in these systems may be identified by other techniques, such as by their rest-frame optical spectra (BPT diagnostics; Baldwin et al. 1981), although we note that the

most heavily obscured can still be missed using these methods (e.g., Stern et al. 2014). However, at present, such spectra are unavailable for the potential counterparts identified here.

5. THE *NUSTAR*-DETECTED POPULATION IN THE CONTEXT OF THE *CHANDRA*-ECDFS SOURCE POPULATION

As we have seen, the majority of our significantly detected *NuSTAR* sources have *Chandra* counterparts. In this section, we consider how the *NuSTAR*-detected population relates to the wider population of X-ray sources previously detected in the *Chandra*-ECDFS survey. First, to explore whether the *Chandra* flux is a strong predictor of whether a source is detected by *NuSTAR* (as would be expected), we first plot the distribution of *Chandra* 3–8 keV fluxes for each source in the L05 catalog against the mean *NuSTAR* exposure time at that position, highlighting those that are detected in each of our three *NuSTAR* bands (i.e., 3–8, 8–24, 3–24 keV; see Figure 15). This plot indeed shows that the brightest *Chandra* sources are preferentially detected by *NuSTAR*, with 24 of the 34 sources (i.e., 71%) with *Chandra*-measured $F_{3\text{-}8 \text{ keV}} > 10^{-14} \text{ erg s}^{-1} \text{ cm}^{-2}$ and *NuSTAR* exposure >50 ks detected in at least one *NuSTAR* band. Of the other 10, four seem to be associated with local minima in the P_{False} maps that lie just above our detection threshold (i.e., having $\log(P_{\text{False}}) > -4.5$, compared to our threshold of ~ -5.2). Thus, while formally undetected, there is at least some evidence of their presence in the *NuSTAR* maps. By contrast, there is no hint of a reduced P_{False} in the *NuSTAR* maps at the positions of the other six bright *Chandra* sources. Five of these lie in regions of the *NuSTAR* maps with comparatively low exposure (i.e., <100 ks), which may explain their nondetection. One, however, lies in a region of relatively high exposure (i.e., ∼190 ks; L05 ID: 577), and thus, with a *Chandra* 3–8 keV flux of $2 \times 10^{-14} \text{ erg s}^{-1} \text{ cm}^{-2}$ and a photon index of 1.67, we would expect it to be detected by *NuSTAR*. One possibility for the lack of *NuSTAR* detection is source variability, with a factor of a few reduction in flux being sufficient to explain the lack of detection. However, with similar fluxes between the *Chandra* and *XMM-Newton* observations (separated by about eight years), this source shows little evidence of strong variability. As such, at present it is not clear why the bright *Chandra* source L05: 577 is not detected by *NuSTAR*.

Comparing between the individual bands in Figure 15, it is evident that the relationship between the *Chandra* 3–8 keV flux and *NuSTAR* detection differs between the *NuSTAR* bands. As expected, detection in the *NuSTAR* 3–8 keV band is strongly related to the *Chandra* 3–8 keV flux, with the vast majority of the detections (25 of 33) in this band having *Chandra*-measured $F_{3\text{-}8 \text{ keV}} > 10^{-14} \text{ erg s}^{-1} \text{ cm}^{-2}$. However, this correspondence between detection and *Chandra* flux is weaker in the 8–24 keV band, with only 11 of the 37 *Chandra* sources with *Chandra*-measured $F_{3-8 \text{ keV}} > 10^{-14} \text{ erg s}^{-1} \text{ cm}^{-2}$ being detected in this harder band. Interestingly, the source with the faintest *Chandra* 3–8 keV counterpart of all the *NuSTAR* sources is detected in the 8–24 keV *NuSTAR* band but not in the 3–8 keV band (*NuSTAR* J033144–2803.0; *NuSTAR*-ECDFS ID: 8; L05 ID: 145). A *NuSTAR* detection in the 8–24 keV band, but not the 3–8 keV band, indicates a hard X-ray photon index, but with a *Chandra*-measured photon index of $\Gamma = 1.51$ for this source, this does not appear to be the
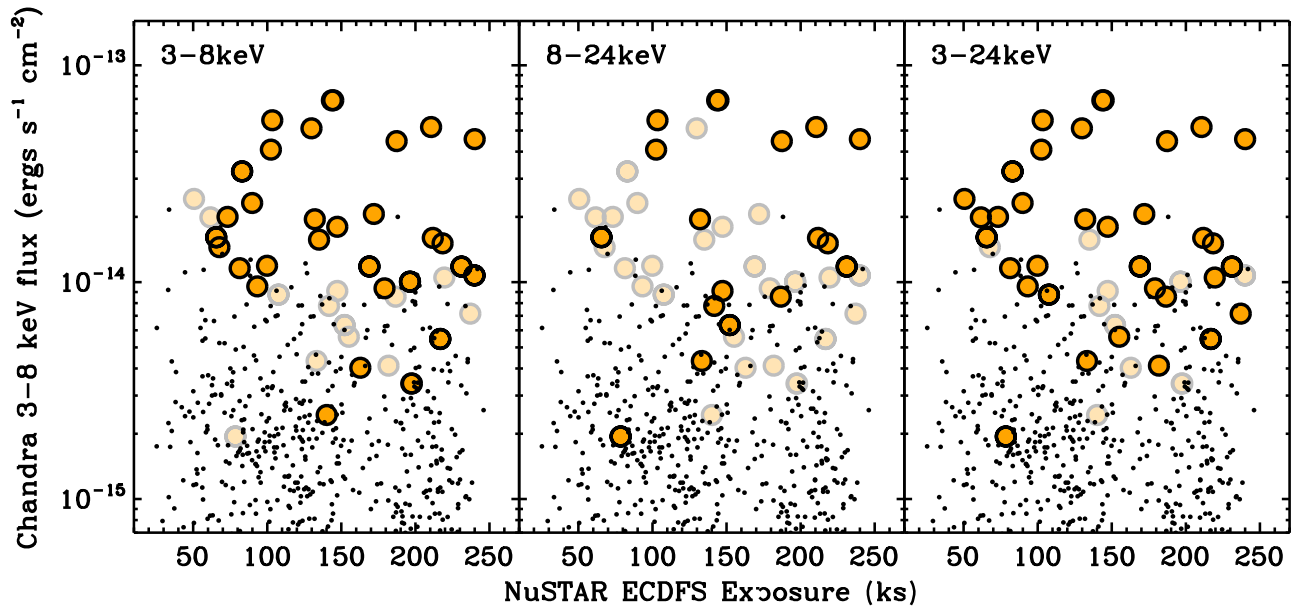
Figure 15. *Chandra*-derived 3–8 keV fluxes for sources in the L05 catalog plotted against the *NuSTAR* exposure time at those positions (small black points). In each panel, we highlight those sources that are detected in the 3–8, 8–24, and 3–24 keV bands (orange points). Lighter points show sources that are detected by *NuSTAR* but not in that specific band. As expected, *NuSTAR* typically detects the brightest sources at a given exposure time, although there are examples of undetected sources interspersed between the detected sources, suggesting that *NuSTAR* detection is not a simple function of source flux and exposure. The reasons for this are explored in Section 5.

case. Again, we checked for possible counterparts in the later *XMM-Newton* observations of the field, but found none (i.e., it is undetected in the *XMM-Newton* 2–10 keV band), so we are unable to rule out source variability as an explanation for the *NuSTAR* detection of this comparatively faint *Chandra* source. We do note, however, that the next faintest *Chandra* source detected in the *NuSTAR* 8–24 keV band does have a very hard *Chandra*-derived photon index of $\Gamma = -0.72$ (NuSTAR J033145–2745.2; NuSTAR-ECDFS ID: 9; L05 ID: 152), which would explain its strong detection in this band.

In light of this faint, but very hard photon index *Chandra* source being detected with *NuSTAR*, we explore what bearing the *Chandra*-derived hardness ratio (the 2–8 to 0.5–2 keV ratio) has on *NuSTAR* detections in general. For this, we plot the *Chandra*-derived hardness ratio against *Chandra*-derived 3–8 keV fluxes for sources detected in the ECDFS survey (L05), highlighting those that are detected by *NuSTAR* (see Figure 16). Here, we only plot sources with >50 ks of *NuSTAR* coverage. For those *NuSTAR* sources with multiple *Chandra* counterparts, we plot the hardness ratio derived from summing the 2–8 to 0.5–2 keV band counts from all counterparts and the sum of their 3–8 keV fluxes. From this plot, there is no strong evidence that sources detected in the *NuSTAR* 8–24 keV band are preferentially those with harder X-ray spectra (based on *Chandra* hardness ratios). Indeed, the majority (five of eight) of sources detected in the *NuSTAR* 8–24 keV band but not the 3–8 keV band have a hardness ratio *below* the median value for all *Chandra* ECDFS sources (i.e., 0.85). This also holds for *all NuSTAR* sources detected in the 8–24 keV band, not just those that are not also detected at 3–8 keV (15 of 22 have hardness ratios below the median value). As such, based on this analysis, we find no strong evidence that the *Chandra* hardness ratio has a strong bearing on whether a source is detected by *NuSTAR*, although we acknowledge our relatively small sample size. Source
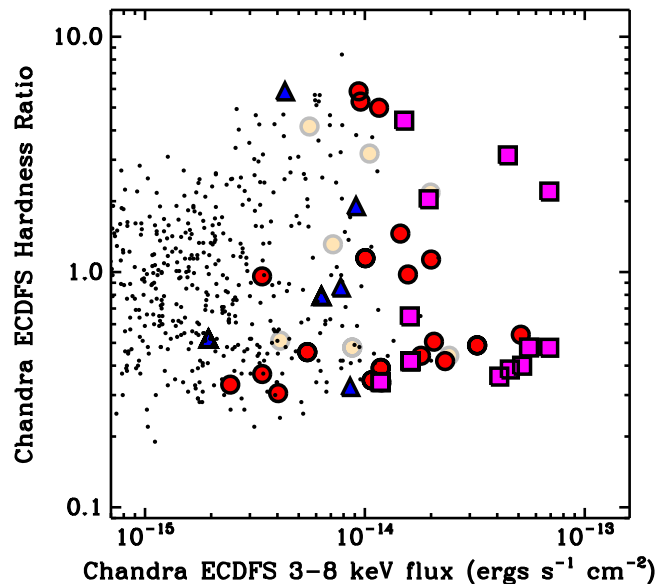

Figure 16. Plot of *Chandra*-derived 2–8 keV to 0.5–2 keV hardness ratio against *Chandra*-measured 3–8 keV flux for detected *Chandra* sources in the ECDFS (small points). Highlighted are those sources that are detected by *NuSTAR* in the 3–8 keV band but not the 8–24 keV band (red circles), those that are detected in the 8–24 keV band but not the 3–8 keV band (blue triangles), those that are detected in both the 3–8 and 8–24 keV bands (magenta squares), and those that are only detected in the single 3–24 keV band (faint circles). For those *NuSTAR* sources with multiple *Chandra* counterparts, we plot the hardness ratio derived from summing the 2–8 to 0.5–2 keV band counts from all counterparts and the sum of their 3–8 keV fluxes. While there is a clear tendency for the *NuSTAR*-detected sources to be the brightest *Chandra* sources, as expected, there is no clear connection between the *Chandra*-derived hardness ratio and whether a source is detected by *NuSTAR* at 8–24 keV.

variability may be able to explain some of this effect, although another possibility is that simple *Chandra* hardness ratios are a

poor proxy for the true spectral properties of the X-ray sources detected by *NuSTAR*. Ascertaining whether this is indeed the case will be the focus of future papers exploring the spectral properties of these *NuSTAR* sources in detail.

6. SUMMARY

In this paper we have described the *NuSTAR* survey of the ECDFS and presented the first results from considering the population of sources detected by *NuSTAR* in this field. Such blank field surveys are a crucial first step in determining the number counts (i.e., log N–log S) and luminosity function of the resolved hard X-ray (>8 keV) source population, which will be the focus of two future papers (B. Harrison et al. 2015, in preparation; J. Aird et al. 2015, in preparation, respectively). With a maximum unvignetted exposure of ≈ 360 ks, the ECDFS currently represents the deepest contiguous component of the *NuSTAR* extragalactic survey, reaching sensitivity limits of $\approx 1.3 \times 10^{-14}$ erg s^{-1} cm^{-2} (3–8 keV), $\approx 3.4 \times 10^{-14}$ erg s^{-1} cm^{-2} (8–24 keV), and $\approx 3.0 \times 10^{-14}$ erg s^{-1} cm^{-2} (3–24 keV). Our main results from this first paper looking at the population of *NuSTAR* sources detected in the ECDFS can be summarized as follows.

1. Within the full $\sim 30' \times 30'$ ECDFS, we detect 54 *NuSTAR* sources, although only 49 of these remain significant after the effects of neighboring sources are taken into account (after deblending). Nineteen of these 49 are detected in the 8–24 keV band, the energy range uniquely probed by *NuSTAR* to unprecedented depths (see Section 3.1).
2. Twelve sources are detected in both the 3–8 and 8–24 keV energy bands, enabling us to determine their hardness ratios and, correspondingly, estimate their photon indices within this energy range. The 12 sources display photon indices that span a broad range of values, that is, $\Gamma = 0.5-2.3$, with a median of $\Gamma = 1.70 \pm 0.52$. By adopting a Monte Carlo approach to sample the band ratio probability distribution function of all 49 detected sources, we calculate the median photon index for the whole sample as $\Gamma = 1.90 \pm 0.53$ (see Section 3.1).
3. All but three of the 49 significantly detected *NuSTAR* sources have X-ray counterparts in either the *Chandra* or *XMM-Newton* surveys of the ECDFS. The redshifts of these counterparts span the range $z = 0.21-2.7$, which, when combined with their *NuSTAR* fluxes, corresponds to a 10–40 keV luminosity range for our deblended sample of ($\approx 0.7-300) \times 10^{43}$ erg s^{-1}. As such, our *NuSTAR* sample probes below the knee of the extrapolated X-ray luminosity function at $z < 1$ (see Sections 3.1, 3.2).
4. Of the three *NuSTAR* sources without *Chandra* or *XMM-Newton* counterparts, only one shows evidence of AGN signatures at other wavelengths (i.e., via infrared SED fitting; see Section 4).
5. As expected, a high *Chandra* 3–8 keV flux is a good predictor as to whether a source will be detected in other *NuSTAR* bands. However, it is not a 1:1 correlation, with some of the brightest *Chandra* sources not being detected at higher energies with *NuSTAR*. The reason for this is currently unclear because the *Chandra*-derived hardness ratio seems to have very little bearing on whether a source is detected in a given *NuSTAR* band (see

Section 5), but source variability may provide some explanation.

APPENDIX
CATALOG DESCRIPTION

The final catalog of 54 sources generated using the procedure outlined above is available in the form of an electronic table. A summary of the columns of this table is given in Table 3, which we expand upon here:

Column 1: the unique *NuSTAR* ECDFS identification number. Sources are arranged in R.A. order. Multiple rows labeled with the same identifier correspond to where one *NuSTAR* source is matched to more than one *Chandra* source within 30″.

Column 2: the unique name of the *NuSTAR* source, following the IAU-approved naming convention for *NuSTAR* sources: NuSTAR JHHMMSS ± DDMM.m, where m is the truncated fraction of an arcminute in decl. for the arcseconds component.

Columns 3, 4: the R.A. and decl. of the *NuSTAR* source. The position is that of the pixel with the lowest P_{False} in the 20″-smoothed maps across all bands. The position is taken from the band showing the lowest P_{False} (i.e., the band in which the source is most significantly detected). All following photometry and so on is then performed at this one position in all three bands.

Table 3
Overview of Columns in the *NuSTAR* ECDFS Source Catalog

Column	Description
1	Unique NuSTAR ECDFS survey source identification number
2	Name of *NuSTAR* source
3, 4	R.A. and decl. of the *NuSTAR* source
5–7	Flag indicating in which of the three standard bands the source is detected
8–10	Flag indicating in which of the three standard bands the source is detected post-deblending
11–14	Logarithm of the undeblended false probability in the three standard bands
15–16	Logarithm of the deblended false probability in the three standard bands
17	Flag indicating whether the source remains significant post-deblending
18–32	Total, background, and net source counts and associated errors in the three standard bands
33–44	Deblended total, background, and net source counts and associated errors in the three standard bands
45–47	Effective exposure times for the three standard bands
48–62	Total, background, and net source count rates and associated errors in the three standard bands
63–68	Deblended total, background, and net source count rates and associated errors in the three standard bands
69–73	Band ratio; mean, median, mode, and upper and lower limits returned by BEHR algorithm
74–76	Effective photon index and upper and lower limits
77–82	Derived fluxes in the three standard bands
83–88	Derived deblended fluxes in the three standard bands
89	Counterpart catalog code (L05: Lehmer et al. 2005; R13: Ranalli et al. 2013, X11: Xue et al. 2011)
90	Unique identification number of the associated source in the counterpart catalog
91, 92	R.A. and decl. of the associated in the counterpart catalog
93	Separation between the *NuSTAR* position and the associated source in the counterpart catalog
94	3–8 keV *Chandra* or *XMM-Newton* flux of the associated source in the counterpart catalog
95	Combined 3–8 keV or *Chandra* or *XMM-Newton* flux of all associated sources within $30''$ of the *NuSTAR* position
96	Spectroscopic redshift of the associated source in the counterpart catalog
97	Photometric redshift of the associated source in the counterpart catalog
98	Adopted redshift
99, 100	Non-absorption-corrected rest-frame 10–40 keV luminosity and associated error of the *NuSTAR* source
101	Source notes

(This table is available in its entirety in FITS format.)

Columns 5–7: binary flag indicating in which of the three standard bands the source is formally detected (i.e., meets our final thresholds of $\log(P_{\mathrm{False}}) \leqslant -5.19$, $\leqslant -5.22$ and $\leqslant -5.34$ in the 3–8, 8–24, and 3–24 keV bands, respectively). Here and throughout the table, the 3–8, 8–24, and 3–24 keV bands are abbreviated to SB, HB, and FB, respectively.

Columns 8–10: the same as columns 5–7, but after photon counts from neighboring sources have been excluded (i.e., deblending; see Section 2.3.2).

Columns 11–13: the logarithm of P_{False} ($\log(P_{\mathrm{False}})$) in each of the three standard bands based on a $20''$ smoothing length, the smoothing length adopted to assess whether a source is significantly detected (see Section 2.3.1).

Columns 14–16: the same as columns 11–13, but after photon counts from neighboring sources have been excluded (i.e., deblending; see Section 2.3.2).

Column 17: binary flag indicating whether the *NuSTAR* source remains significant in at least one of the standard bands post-deblending.

Columns 18–32: non-aperture-corrected total, background, and net source counts based on $30''$ aperture photometry centered on the position in columns 3, 4 in each of the three standard bands. Errors are given on the total and net counts and are calculated using Gehrels (1986) (see Section 2.3.2). We indicate those sources where the photometric measurement in a given band is $<3\sigma$ with a negative value for the error.

Columns 33–44: same as columns 18–32, but after source counts from neighboring sources have been taken into account (still based on $30''$ aperture photometry). Errors are given on the net counts.

Columns 45–47: mean effective exposure times in $30''$ apertures centered on the position in columns 3, 4 in each of the three standard bands. Unit: s.

Columns 48–62: non-aperture-corrected total, background, and net source count rates, calculated from the source counts in columns 18–32 and the respective mean effective exposure times in columns 45–47. Errors are propagated from those on the source counts, assuming zero error on the effective exposure times. Again, negative error values indicate those sources that are detected at $<3\sigma$ in a given band. Unit: s^{-1}.

Columns 63–68: same as columns 48–62, but after the effects of source blending have been taken into account (calculated using the source counts given in columns 33–44 and respective mean effective exposure times given in columns 45–47). Unit: s^{-1}.

Columns 69–73: 8–24 to 3–8 keV band ratios output by the BEHR algorithm. Because this algorithm is a Bayesian estimator, it calculates the band ratio probability distribution function and provides the mean, median, mode, and upper and lower 68th percentiles, which we report here.

Columns 74–76: effective observed (non-absorption-corrected) photon index of the *NuSTAR* source derived from the mean band ratio and the upper and lower limits given in columns 69–73 (see Section 2.3.3).

Columns 77–82: observed-frame, aperture-corrected source fluxes in the three standard bands. Fluxes are derived from net count rates (columns 48–62) following the procedure outlined in Section 2.3.3. Errors are propagated using the same conversion factors. Again, negative error values indicate those

sources that are detected at $<3\sigma$ in a given band. Units: erg s^{-1} cm^{-2}

Columns 83–88: same as columns 77–82, but after the effects of source blending have been taken into account (using the deblended count rates in columns 63–68).

Columns 89: code indicating the catalog in which a *Chandra* or *XMM-Newton* counterpart to the *NuSTAR* source was identified. L05: Lehmer et al. (2005); R13: Ranalli et al. (2013); X11: Xue et al. (2011).

Column 90: unique identifier of the matched *Chandra* or *XMM-Newton* source(s) from the catalog indicated in column 89 ("recno" in the L05 and X11 catalogs; "ID210" in the R13 catalog). Where there is more than one match within 30″ of the *NuSTAR* position, we provide separate matches on additional table rows. Such multiple matches can therefore be identified by the replication of the *NuSTAR* index in column 1.

Columns 91, 92: R.A. and decl. of the respective *Chandra* or *XMM-Newton* match(es).

Column 93: separation between the *NuSTAR* source and the matched *Chandra* or *XMM-Newton* source. Unit: arcsecond.

Column 94: observed-frame 3–8 keV fluxes derived from the *Chandra* or *XMM-Newton* data. Note: these data are *not* provided in the catalogs of L05, Ranalli et al. (2013), or Xue et al. (2011) because the 3–8 keV band is not a standard band of those papers. Instead, the 3–8 keV fluxes were calculated using ACIS Extract (Broos et al. 2010) with a simple power-law model. Units: erg s^{-1} cm^{-2}.

Column 95: total combined observed-frame 3–8 keV fluxes of *all Chandra* or *XMM-Newton* sources within 30″ of the *NuSTAR* source. Units: erg s^{-1} cm^{-2}.

Column 96: spectroscopic redshift of the matched *Chandra* (from Silverman et al. 2010) or *XMM-Newton* (from Ranalli et al. 2013) source, where available.

Column 97: photometric redshift of the matched *Chandra* (from Silverman et al. 2010) or *XMM-Newton* (from Ranalli et al. 2013) source, where available.

Column 98: the adopted redshift used to calculate the rest-frame 10–40 keV luminosity of the *NuSTAR* source. In cases where both spectroscopic and photometric redshifts are available, we always adopt the spectroscopic redshift.

Columns 99, 100: derived rest-frame 10–40 keV luminosities of the *NuSTAR* sources and associated errors for sources where a redshift is available (either photometric of spectroscopic). Luminosities are calculated using the observed 8–24 keV band flux, and *k-corrections* are performed assuming a photon index of $\Gamma = 1.8$ (see Section 2.3.4). Where a *NuSTAR* source is matched to more than one *Chandra* or *XMM-Newton* source (and therefore may have more than one associated redshift), we provide the 10–40 keV luminosity assuming each of the various available redshifts. Errors are propagated directly from the errors on the 8–24 keV fluxes (i.e., we assume zero error on the redshift). Again, negative error values indicate those sources that are detected at $<3\sigma$ in a given band. Units: erg s^{-1}.

Column 101: any special notes associated with the source.

REFERENCES

Aird, J., Nandra, K., Laird, E. S., et al. 2010, MNRAS, 401, 2531
Ajello, M., Alexander, D. M., Greiner, J., et al. 2012, ApJ, 749, 21
Ajello, M., Greiner, J., Kanbach, G., et al. 2008, ApJ, 678, 102
Akylas, A., Georgakakis, A., Georgantopoulos, I., Brightman, M., & Nandra, K. 2012, A&A, 546, A98
Alexander, D. M., Bauer, F. E., Brandt, W. N., et al. 2003, AJ, 126, 539
Alexander, D. M., & Hickox, R. C. 2012, NewAR, 56, 93
Alexander, D. M., Stern, D., Del Moro, A., et al. 2013, ApJ, 773, 125
Baldwin, J. A., Phillips, M. M., & Terlevich, R. 1981, PASP, 93, 5
Ballantyne, D. R. 2014, MNRAS, 437, 2845
Ballantyne, D. R., Draper, A. R., Madsen, K. K., Rigby, J. R., & Treister, E. 2011, ApJ, 736, 56
Ballantyne, D. R., Everett, J. E., & Murray, N. 2006, ApJ, 639, 740
Baumgartner, W. H., Tueller, J., Markwardt, C. B., et al. 2013, ApJS, 207, 19
Bertin, E., & Arnouts, S. 1996, A&AS, 117, 393
Bonzini, M., Mainieri, V., Padovani, P., et al. 2012, ApJS, 203, 15
Bottacini, E., Ajello, M., & Greiner, J. 2012, ApJS, 201, 34
Brandt, W. N., & Alexander, D. M. 2015, A&ARv, 23, 1
Broos, P. S., Townsley, L. K., Feigelson, E. D., et al. 2010, ApJ, 714, 1582
Brusa, M., Comastri, A., Gilli, R., et al. 2009, ApJ, 693, 8
Burlon, D., Ajello, M., Greiner, J., et al. 2011, ApJ, 728, 58
Cardamone, C. N., Urry, C. M., Damen, M., et al. 2008, ApJ, 680, 130
Cardamone, C. N., van Dokkum, P. G., Urry, C. M., et al. 2010, ApJS, 189, 270
Churazov, E., Sunyaev, R., Revnivtsev, M., et al. 2007, A&A, 467, 529
Civano, F., Elvis, M., Brusa, M., et al. 2012, ApJS, 201, 30
Civano, F., Hickox, R. C., Puccetti, S., et al. 2015, ApJ, in press
Comastri, A., Setti, G., Zamorani, G., & Hasinger, G. 1995, A&A, 296, 1
Damen, M., Labbé, I., van Dokkum, P. G., et al. 2011, ApJ, 727, 1
Del Moro, A., Alexander, D. M., Mullaney, J. R., et al. 2013, A&A, 549, A59
Del Moro, A., Mullaney, J. R., Alexander, D. M., et al. 2014, ApJ, 786, 16
della Ceca, R., Castelli, G., Braito, V., Cagnoni, I., & Maccacaro, T. 1999, ApJ, 524, 674
Donley, J. L., Koekemoer, A. M., Brusa, M., et al. 2012, ApJ, 748, 142
Donley, J. L., Rieke, G. H., Pérez-González, P. G., Rigby, J. R., & Alonso-Herrero, A. 2007, ApJ, 660, 167
Elvis, M., Civano, F., Vignali, C., et al. 2009, ApJS, 184, 158
Freeman, P. E., Kashyap, V., Rosner, R., & Lamb, D. Q. 2002, ApJS, 138, 185
Frontera, F., Orlandini, M., Landi, R., et al. 2007, ApJ, 666, 86
Gandhi, P., Horst, H., Smette, A., et al. 2009, A&A, 502, 457
Gehrels, N. 1986, ApJ, 303, 336
Georgakakis, A., Nandra, K., Laird, E. S., Aird, J., & Trichas, M. 2008, MNRAS, 388, 1205
Giacconi, R., Gursky, H., Paolini, F. R., & Rossi, B. B. 1962, PhRvL, 9, 439
Gilli, R., Comastri, A., & Hasinger, G. 2007, A&A, 463, 79
Gilli, R., Salvati, M., & Hasinger, G. 2001, A&A, 366, 407
Goulding, A. D., Forman, W. R., Hickox, R. C., et al. 2012, ApJS, 202, 6
Gruber, D. E., Matteson, J. L., Peterson, L. E., & Jung, G. V. 1999, ApJ, 520, 124
Harrison, F. A., Craig, W. W., Christensen, F. E., et al. 2013, ApJ, 770, 103
Hasinger, G. 2008, A&A, 490, 905
Hickox, R. C., & Markevitch, M. 2006, ApJ, 645, 95
Hsieh, B.-C., Wang, W.-H., Hsieh, C.-C., et al. 2012, ApJS, 203, 23
Krivonos, R., Revnivtsev, M., Lutovinov, A., et al. 2007, A&A, 475, 775
Lacy, M., Storrie-Lombardi, L. J., Sajina, A., et al. 2004, ApJS, 154, 166
Laird, E. S., Nandra, K., Georgakakis, A., et al. 2009, ApJS, 180, 102
Lehmer, B. D., Brandt, W. N., Alexander, D. M., et al. 2005, ApJS, 161, 21
Lehmer, B. D., Xue, Y. Q., Brandt, W. N., et al. 2012, ApJ, 752, 46
Luo, B., Bauer, F. E., Brandt, W. N., et al. 2008, ApJS, 179, 19
Lutz, D., Poglitsch, A., Altieri, B., et al. 2011, A&A, 532, A90
Madau, P., Ghisellini, G., & Fabian, A. C. 1994, MNRAS, 270, L17
Magnelli, B., Popesso, P., Berta, S., et al. 2013, A&A, 553, A132
Marshall, F. E., Boldt, E. A., Holt, S. S., et al. 1980, ApJ, 235, 4
Mullaney, J. R., Alexander, D. M., Goulding, A. D., & Hickox, R. C. 2011, MNRAS, 414, 1082
Mushotzky, R. F., Cowie, L. L., Barger, A. J., & Arnaud, K. A. 2000, Natur, 404, 459
Paolillo, M., Schreier, E. J., Giacconi, R., Koekemoer, A. M., & Grogin, N. A. 2004, ApJ, 611, 93
Park, T., Kashyap, V. L., Siemiginowska, A., et al. 2006, ApJ, 652, 610
Ranalli, P., Comastri, A., Vignali, C., et al. 2013, A&A, 555, A42
Scoville, N., Aussel, H., Brusa, M., et al. 2007, ApJS, 172, 1
Setti, G., & Woltjer, L. 1989, A&A, 224, L21
Silverman, J. D., Mainieri, V., Salvato, M., et al. 2010, ApJS, 191, 124
Stern, D., Eisenhardt, P., Gorjian, V., et al. 2005, ApJ, 631, 163
Stern, D., Lansbury, G. B., Assef, R. J., et al. 2014, ApJ, 794, 102
Tomsick, J. A., Gotthelf, E. V., Rahoui, F., et al. 2014, ApJ, 785, 4
Tozzi, P., Rosati, P., Nonino, M., et al. 2001, ApJ, 562, 42
Treister, E., & Urry, C. M. 2005, ApJ, 630, 115

Treister, E., Urry, C. M., & Virani, S. 2009, ApJ, 696, 110
Tueller, J., Mushotzky, R. F., Barthelmy, S., et al. 2008, ApJ, 681, 113
Ueda, Y., Akiyama, M., Hasinger, G., Miyaji, T., & Watson, M. G. 2014, ApJ, 786, 104
Ueda, Y., Takahashi, T., Inoue, H., et al. 1999, ApJ, 518, 656
Vasudevan, R. V., Mushotzky, R. F., & Gandhi, P. 2013, ApJL, 770, L37

Wik, D. R., Hornstrup, A., Molendi, S., et al. 2014, ApJ, 792, 48
Worsley, M. A., Fabian, A. C., Bauer, F. E., et al. 2005, MNRAS, 357, 1281
Xue, Y. Q., Luo, B., Brandt, W. N., et al. 2011, ApJS, 195, 10
Xue, Y. Q., Wang, S. X., Brandt, W. N., et al. 2012, ApJ, 758, 129
Young, M., Brandt, W. N., Xue, Y. Q., et al. 2012, ApJ, 748, 124